Published in final edited form as:
Contrast Media Mol Imaging. 2011 ; 6(5): 346–369. doi:10.1002/cmmi.455.

Advanced contrast nanoagents for photoacoustic molecular imaging, cytometry, blood test and photothermal theranostics†

Adam de la Zerda[a,b,*], **Jin-Woo Kim**[c,*], **Ekaterina I. Galanzha**[d], **Sanjiv S. Gambhir**[a,e], and **Vladimir P. Zharov**[d,*]

[a]Molecular Imaging Program at Stanford, the Bio-X Program and the Department of Radiology, Stanford University, Palo Alto, CA, USA

[b]Department of Electrical Engineering, Stanford University, Palo Alto, CA, USA

[c]Bio/Nano Technology Laboratory, Department of Biological and Agricultural Engineering and Institute for Nanoscience and Engineering, University of Arkansas, Fayetteville, AR, USA

[d]Phillips Classic Laser and Nanomedicine Laboratories, University of Arkansas for Medical Sciences, Little Rock, AR, USA

[e]Departments of Bioengineering and Materials Science and Engineering, Stanford University, Palo Alto, CA, USA

Abstract

Various nanoparticles have raised significant interest over the past decades for their unique physical and optical properties and biological utilities. Here we summarize the vast applications of advanced nanoparticles with a focus on carbon nanotube (CNT)-based or CNT-catalyzed contrast agents for photoacoustic (PA) imaging, cytometry and theranostics applications based on the photothermal (PT) effect. We briefly review the safety and potential toxicity of the PA/PT contrast nanoagents, while showing how the physical properties as well as multiple biological coatings change their toxicity profiles and contrasts. We provide general guidelines needed for the validation of a new molecular imaging agent in living subjects, and exemplify these guidelines with single-walled CNTs targeted to $\alpha_V\beta_3$, an integrin associated with tumor angiogenesis, and golden carbon nanotubes targeted to LYVE-1, endothelial lymphatic receptors. An extensive review of the potential applications of advanced contrast agents is provided, including imaging of static targets such as tumor angiogenesis receptors, *in vivo* cytometry of dynamic targets such as circulating tumor cells and nanoparticles in blood, lymph, bones and plants, methods to enhance the PA and PT effects with transient and stationary bubble conjugates, PT/PA Raman imaging and multispectral histology. Finally, theranostic applications are reviewed, including the nanophotothermolysis of individual tumor cells and bacteria with clustered nanoparticles,

†This article is published in Contrast Media and Molecular Imaging as part of the special issue on Photoacoustic Imaging, edited by Dr. Gregory Lanza, Department of Medicine, Washington University Medical Hospital.

*Correspondence to: A. de la Zerda, Molecular Imaging Program at Stanford, the Bio-X Program and the Departments of Electrical Engineering and Radiology, Stanford University, Palo Alto, CA, USA. adlz@stanford.edu. J.-W. Kim, Bio/Nano Technology Laboratory, Department of Biological and Agricultural Engineering and Institute for Nanoscience and Engineering, University of Arkansas, Fayetteville, AR, USA. jwkim@uark.edu. V. P. Zharov, Phillips Classic Laser and Nanomedicine Laboratories, University of Arkansas for Medical Sciences, Little Rock, USA. zharovvladimirp@uams.edu.

nanothrombolysis of blood clots, detection and purging metastasis in sentinel lymph nodes, spectral hole burning and multiplex therapy with ultrasharp rainbow nanoparticles.

Keywords

photoacoustic molecular imaging; photothermal theranostics; nanotechnology; carbon nanotubes; flow cytometry; blood test; cancer; metastasis

1. INTRODUCTION – HISTORICAL BACKGROUND

Recent advances in photothermal (PT) and photoacoustic (PA) techniques based on nonradiative conversion of absorbed energy in thermal and accompanying acoustic or bubble phenomena demonstrated a great potential in various spectroscopic sensing, imaging and therapy applications (1–3). The PT and PA techniques use either endogenous biomolecules with natural PT/PA contrast properties (e.g. hemoglobin, melanin, cytochromes or carotenoids), or exogenous contrast agents. Such exogenous agents may be small molecule optical dyes including Evans blue, indocyanin green (ICG), lymphazurin, and methylene blue, as well as synthetic nanoparticles (NPs) such as gold and carbon-based NPs (2). While the primary advantage of small molecules is their favorable bio-distribution and clearance rates from the body, NPs typically exhibit much higher optical absorption and photostability.

Numerous biomedical applications of single-walled and multi- walled carbon nanotubes (SWNTs and MWNTs, respectively, or CNTs in general) have been demonstrated over the years. Owing to their ability to absorb light at a wide range of wavelengths spanning the ultra-violet, visible near infra-red (NIR) and microwave spectral ranges, CNTs are natural contrast agents for PA and PT technique. The first demonstration of CNTs as PA contrast agents was performed by Zharov *et al.* in 2007 through *in vitro* and *in vivo* detection of circulating CNTs alone, or through circulating *Staphylococcus aureus* and *Escherichia coli* labeled with CNTs in blood flow using a novel *in vivo* flow cytometry device called a PA/PT flow cytometry (PAFC/PTFC) system (4). At the same time, real-time two-color PAFC was applied for *in vivo* identification of CNTs in lymph flow (5). In 2008, de la Zerda *et al.* demonstrated the first *in vivo* PA imaging of CNTs by molecularly targeting SWNTs to tumor neovasculature using arginine–glycine–aspartic acid (RGD) peptides in living mice (6). Since then, multiple groups have proposed various chemical modifications to CNTs that enhance their PA signals, as well as demonstrating new applications of the PA technique using CNTs. Chemical modifications included coating of CNTs with organic optical dyes (7), gold with folates and antibodies for molecular targeting of circulating tumor cells (CTCs) and endothelial lymphatic LYVE-1 receptors with potentially lower toxicity (8,9), or antibodies for targeting the primary tumor (14). CNTs were also suggested as potential contrast agents for sentinel lymph nodes (SLNs) imaging (9–13). SWNTs were shown to absorb microwaves at 3 GHz frequency thereby, leading to a thermoacoustic signal in response (13). Other applications of CNT include PA detection of metastasis in SLNs (9,10), as well as identification of tumor-initiating cancer stem cells in circulation among bulk CTCs (25). Recently novel cytometry methods based on PT and PA Raman spectroscopy were demonstrated for the detection of nonlinear effects in CNTs *in vivo* (15). Both PT and

PA microscopy have shown great promise for studying distribution of CNTs in histological samples (16) and, most recently, in plants (17), where such visualization of CNTs in plants can lead to to better understanding of plant–CNT interactions. For *in vivo* cytometry applications, a nanosecond fiber 1064 nm laser with a 0.5 MHz repetition rate enabled the detection of fast-flowing CNTs *in vivo* and *in vitro* with velocities of up to 2.5 m/s (18).

Beyond purely imaging and sensing, the PT and PA effects in CNTs can be further used for therapy. In 2003, Zharov's laboratory demonstrated pulsed PT nanotherapy (termed also nanophotothermolysis), with laser-induced nano- and micro-bubbles around overheated gold NPs, particularly NP clusters, which eventually led to the death of tumor cells or bacteria (19–26). The same laboratory also proposed using NPs for targeting bones, atherosclerotic plaques, blood, lymph vessels (27,117) and thrombus (see below). Strong acoustic and explosion effects (e.g. shock waves) (27) can be used for differentiation of multipotent marrow stromal cells and nonthermal localized destruction of cells (28,29). Compared with continuous wave (CW) laser PT treatment of tumors (30,31), a laser in pulsed mode has the potential to precisely kill individual cancer cells with a spatial accuracy of a few micrometers without harmful effects to the surrounding healthy cells (19,32). The PT therapy and PA sensing or imaging are based on similar thermal effects, which allow their integration into a multifunctional theranostic system using PA/PT responses for navigation, optimization and monitoring the efficiency of PT nanotherapy. In particular, laser-induced nano- and microbubbles provide both amplification of the PT and PA effects and sharpening of the spectra peaks. This results in the increased sensitivity, specificity and capability of multiplex PT therapy by targeting multiple NPs with different optical spectra to different disease-associated biomarkers (8,33). In this article, we emphasize our findings in the application of PT/PA technologies using bare, functionalized and hybrid CNTs and their nano- and micro-clusters.

2. OPTIMIZATION OF NANOPARTICLES FOR PT AND PA APPLICATIONS

2.1. Conditions for PT/PA contrast agents, surrounding medium, and laser excitation

To provide an effective transfer of laser energy into PT and PA signals in absorbing media, several conditions that govern the physical processes of energy conversion (i.e. excitation → nonradiative relaxation → heating → acoustic wave and in some cases, bubble formation) should be met. The two key conditions that must be met are the thermal and stress conditions (1–4). Additional conditions with regard to contrast to background and dynamic situations (34–36), where laser pulse rates are high and/or for fast moving targets, are described below.

2.1.1. Optical conditions—The absorbed laser energy in NPs, W_{NP}, should be greater than the absorbed energy, W_B, in surrounding tissue within the detected volume, i.e.

$$W_{NP}/W_B = \sigma_{NP} N/a_B V_B > 1 \quad (1)$$

where σ_{NP} is the absorption cross section of the NPs, N is number of NPs in the detected volume V_B, and a_B is the absorption coefficient of the background tissue (34,35). Thus, for

strongly absorbing NPs with $\sigma_B \approx 10^{-10}$ cm^2, the single NP can be detectable in absorption background in NIR range at typical level of a_B of 0.1 cm^{-1} (lymphatics) or ~2 cm^{-1} (blood) in the volume V_B with linear size L ($V_B \approx L^3$) of 10 and 3.7 μm, respectively. Thus, single NP can be detected in the superficial tissue and microvessels in the small volume with minimum background absorption provided either by strong focusing of laser beam or using a high-frequency focused ultrasound transducer with small focal volume (4,32). In the larger detected volume, a greater NP number needs to be detected (e.g. $N = 10^3$ for V with L ~100 μm). The detection sensitivity can be enhanced 10- to 100-fold by nonlinear amplification of PT/PA signals through laser-induced nanobubble formation around overheated NPs (33). These rough estimations are in line with our experimental data demonstrating imaging (19) and detection (4) of just single and few gold NPs (or one small NP clusters) in a single cell or superficial blood microvessels, especially between individual erythrocytes in the capillary. In order to minimize the number of NPs required for detection, a strongly focused laser beam may be used, as well as the use of a high-frequency focused ultrasound transducer with small focal volume. On the other hand, a very high W_{NP} may result in undesired light attenuation by strongly absorbing and scattering NPs or bubble formation around the NPs (33).

2.1.2. Relaxation conditions—To provide maximal PT and PA effects, most absorbed energy should be transformed into heat, which occurs at:

$$\tau_{NR} < \tau_R \quad (2)$$

where τ_{NR} and τ_R are the characteristic times of nonradiative and radiative relaxation, respectively. In most NPs, this condition is fulfilled ($\tau_{NR} \approx 10^{-12}$ to 10^{-11}s, $\tau_R \approx 10^{-8}$ to 10^{-10}s), while in some dyes it is not (4). This together with the relatively low absorption cross section of fluorescent agents renders them less effective as PT/PA contrast agents compared with NPs. Nevertheless, the high sensitivity of the PT/PA technique provides imaging of even single quantum dots (33,34). As proposed in Shashkov *et al.* (34), the contrast of dyes can be enhanced by their conjugation with metal NPs because of quenching effects in dye–metal interfaces. Relaxation conditions at $t_P \leq \tau_{NR}$ may provide a study of ultrafast relaxation phenomena with ultra-short (femtosecond) laser pulses.

2.1.3. Thermal conditions for single laser pulse—To provide efficient heating of NPs without heat loss, the pulse duration, t_P, should be less than the characteristic thermal relaxation time, τ_T, of NPs:

$$t_P \leq \tau_T \quad (3)$$

The fulfillment of the thermal conditions mean achievement of the maximal value of NP temperature practically without ambient heat exchange. For a solid nanosphere with radius R, $\tau_T = R^2/6.75\,k$, where k is the thermal diffusivity (4). For targets with R = 50 nm, 500 nm, 5 μm, and 50 μm (e.g. NPs, cellular organelles, cells or bulk media with a 100 μm laser spot), τ_T is ~3 ns, 0.3 μs, 30 μs and 3 ms, respectively. In strongly absorbing NPs such as gold or CNTs, the absorbed energy in the NP surface is almost instantaneously (characteristic time ~10^{-12} s) transformed into thermal energy and very quickly averaged in

the absorbing layers. Then the heat transfers from the layers to the core (e.g. in hollow NPs, SWNTs, or nanoshells) and surrounding water or preferentially to water (for solid NPs). For example, the ratio of characteristic times of heat conductivity for water and silica is about 6 (118). Thus, in gold nanoshells the shell and silica core reach thermal equilibrium first, and further NP cooling is due to heat transfer to surrounding water. For hollow metal NPs filled with water or liquids with similar thermal properties, redistribution of heat between the core and surrounding medium is approximately equal. In MWNTs, laser radiation is predominately absorbed in external layers and then heat is redistributed between layers.

For a first approximation many closely located NPs can be considered as an equivalent heated quasi-solid NP with average heat capacity C_{NP} and density ρ_{NP}, and the characteristic thermal relaxation (i.e. cooling) time for heat transfer between the NP surrounding water with the coefficient of thermal conductivity K_W can be estimated as $\tau_T = R^2 \rho_{NP} C_{NP}/nK_W$, where coefficient n (3–6) depends on the NP shape. For example, a gold nanosphere having R = 50 nm in ambient water will exhibit $\tau_T \approx 1.2$ ns. Thus, for a 10 ns laser pulse, the thermal conditions are fulfilled for most large targets, and are not fulfilled for very small NPs. The condition $t_P > \tau_T$ can be used for the heat exchange of NPs with the ambient tissue and its heating. A more rigorous analysis of thermal effects in multilayer NPs can be found elsewhere (35,36).

2.1.4. Thermal conditions for multiple laser pulses—While the previous conditions do not take into account possible temporal overlapping of thermal effects at high laser pulse rate, f_{REP}, this may lead to target overheating and, thus, a decrease in PT and PA signals. To avoid this effect, the thermal conditions for successive laser pulses are defined as:

$$f_{\mathrm{REP}} \leq 1/\tau_T \quad (4)$$

when there is enough time for target cooling before the next pulse comes (18). For the typical targets indicated above, f_{REP}^{MAX} was estimated as ~330 MHz, 3.3 MHz, 33 kHz and 330 Hz, respectively. However, the rapid rise time of PT signals (i.e. temperature increases) (18) may lead to an increase in average medium temperature without decrease in PT signal amplitude, which makes this condition less strict. Thermal conditions [equation (4)] are introduced for noninvasive PA diagnosis. However, for PT therapy, spatial or temporal overlapping of thermal fields from individual NPs can in some cases provide positive effects by increasing average temperature and thus improve PT therapeutic efficiency, especially for large targets (e.g. a tumor).

2.1.5. Acoustic stress conditions for single laser pulse—The transformation of thermal energy into acoustic energy, t_P, should satisfy:

$$t_P \leq \tau_A = 2R/c_S \quad (5)$$

where τ_A is the acoustic relaxation time defined as the transit time of the acoustic wave traveling through a distance of 2R (target diameter) and c_S is the speed of sound (1,2,4). For nanospheres with R = 30 nm in water with $c_s \approx 1.5 \times 10^5$ cm/s, τ_A is in the sub-nanosecond range, ~40 ps. Thus, for broadly used pulsed nanosecond lasers, condition (5) is not quite

fulfilled for small targets, and the PA signal amplitude will decrease (as $\sim \tau_A/t_P$) as the width increases. Nevertheless, strong PA signals were demonstrated from such small NPs using nanosecond laser pulses (4–17). This may be explained by the presence of large NP aggregates, the nonlinear bubble-related amplification of PA signals (18) or appropriate condition for thermal-based generation of acoustic waves in pulse mode (e.g. ultrafast temperature rise).

2.1.6. Acoustic (transducer response) condition for multiple laser pulses—In certain samples, under single laser pulse excitation, a train of acoustic oscillations may be observed, instead of the classic signal shape with single positive and negative components. This is true particularly in those samples with hard acoustic surfaces such as histology slides. The elongated signal oscillation can be estimated through ultrasound transducer response, τ_{TR}, although in fact these responses are associated with acoustic interface properties between transducer and samples.

Overlapping of acoustic waves after ultrasound transducer with time response, τ_{TR}, should also limit f_{REP}^{MAX}

$$f_{\mathrm{REP}} \leq 1/\tau_{\mathrm{TR}} \quad (6)$$

In the presence of acoustic reflections, the recorded acoustic response will be formed by a train of oscillations, whose duration is determined by the transducer and setup parameters. With a τ_{TR} of 0.1–15 μs, f_{REP}^{max} should be less than 10 MHz and 60 kHz, respectively.

2.1.7. Flow conditions—Flow partly eases the thermal conditions for noninvasive diagnosis as it removes excess heat from the laser spot and target site. This may decrease possible target overheating and even photo-damage of the tissues, and facilitate the fulfillment of thermal conditions for multiple laser pulses. For a flowing sample, the lifespan of target in the detected volume is defined as $\tau_F = D_L/v_F$, where D_L is the laser beam or transducer focus size along the blood vessel and v_F is the linear flow velocity. For $\tau_F \leq \tau_T$, f_{REP}^{MAX} could be estimated as $f_{REP}^{MAX} \leq 1/\tau_F$. For example for a flow velocity, v_F, of 50 cm/s (large artery), and a laser beam width, D_L, of 10 μm, f_{REP}^{MAX} can be as high as 50 kHz, compared with 10 kHz in static conditions. For higher flow velocity, the increases in frequency will be even greater. In a fast flow, τ_T may decrease further as additional target cooling takes place owing to local turbulences (122), allowing the use of even higher laser pulse rates (18).

2.1.8. Bubble conditions—Laser-induced nano- and microbubbles around strongly absorbing NPs are important phenomena to increase the sensitivity of PT/PA diagnostics and the efficiency of PT therapy (8–11,19–27,33). Specifically, the vapor blanket (bubble) formation, its expansion and the formation of intense pressure waves can amplify PA signals and result in mechanical damage and rupture of the cells and tissue. Photothermal-based bubbles will be generated at laser pulse energy fluence

$$E > E_{\mathrm{BTH}}, \quad (7)$$

where E_{BTH} is the threshold of energy fluence for bubbles formation around NPs. The analyses of condition for maximal efficacy of bubble formation was performed in (35,36). Below we present selected experimental results including use NP clusters, appropriate surrounding media (e.g. ethanol) and stationary nano- and microbubbles conjugated with NPs.

2.2. Methodology for NP optimization

Based on the models described above, we identified several ways to improve the NP detection limit by increasing conversion of laser energy into PT, PA, and bubble formation phenomena (34–36). In pulse mode, the PA signal is proportional to laser energy, the absorption cross-section, and the coefficient of thermal expansion, and is inversely proportional to density and heat capacity, and is independent of NP volume at fulfilled thermal and acoustic condition (1,2,34). Thus, NPs with higher coefficient of thermal expansion, and lower density and heat parameters, provide higher PA signals at the same NP absorption. In addition, bubble formation, as a PA signal enhancer and a therapy modality, is more effective at a low boiling point, vaporization heat, surface tension and heat capacity, or a higher coefficient of thermal expansion. In particular, lower surface tension results in a lower pressure inside the bubble, required for bubble expansion. An increase in sensitivity could be also achievable by decreasing the laser pulse duration to the picosecond regime (22), which would match better with the thermal and acoustic conditions, since the thermal, τ_{T}, and acoustic, τ_{A}, relaxation times are in the sub-nanosecond range for small NPs. Naturally, doing so may be challenging for technological as well as safety constraints. Alternatively, the thermal relaxation times could be increased by using larger NPs ($\tau_{\mathrm{T}} \propto R^2$, $\tau_{\mathrm{A}} \propto R$); however, targeting large NPs to molecular targets in living animals is challenging.

To improve the PA sensitivity it is suggested to: (1) increase absorbed energy through conjugation of relatively low absorbing NPs (e.g. CNTs) to more strongly absorbing materials, including plasmon gold NPs and conventional dyes such as ICG (see below) (7,9,34); (2) use thermally insulating layers around the optically absorbing part of the NP with low heat diffusion coefficient and thus improve the thermal condition (4,34); (3) use a layer with a high coefficient of thermal expansion (e.g. ethanol) (24,34); (4) use evaporation (9) and explosion (27) effects leading to bubble formation and shock waves that significantly enhance the generation of nonlinear PA signals; and (5) conjugate the NP with nano- and microbubbles to enhance bubble expansion leading to more powerful PA signals and therapeutic effects (unpublished results obtained in 2007 in Zharov's laboratory and presented as the preliminary data in the NIH grant 1RC1CA1464919). It should be noted that hollow nanostructures like CNTs have a lower heat capacity compared with solid NPs, allowing better heating in pulse mode even at the same absorption properties.

2.3. Integrated PA/PT diagnostics and therapy (theranostics) with nanoclusters

To overcome difficulties to deliver large NPs and low PA signals from small NPs, in 2004 we proposed a concept of PA nanodiagnostics and PT nanotherepy (termed also

nanophotothermolysis), which is based on self-assembling small NPs into larger nanoclusters directly in targeted sites of living organisms (20–22). This concept uses relatively small gold NPs (e.g. 5–30 nm) that can be delivered more easily to cancer cells with different methods (physiological transportation, conjugation with antibodies, or viral infection) than larger NPs (22). Smaller NPs also provide lower background in blood and tissue, and can more effectively target biomarkers on cancer cells. After delivery and by providing specific conditions, these NPs are self-assembled into larger nanoclusters (i.e. many closely located NPs) directly on live cancer cells around dense or clustered biomarkers. Such nanoclusters, provide greatly enhanced laser-induced optical, thermal, and acoustic bubble formation phenomena, resulting in linear and nonlinear enhancement of the PT and PA effects (Fig. 1A). These enhancements can be explained by: (1) increase in the cluster's average absorption; (2) better heating efficiency resulting from an enhanced ability to confine the nanosecond laser pulse within the nanocluster's size; (3) a decrease in the bubble-formation threshold; and (4) the overlapping of bubbles from different NPs. Specifically, for gold nanospheres with absorbance peak at ~525 nm, the creation of nanoclusters leads to a significant red-shift to ~700–1100 nm (20–22). This allows the use of small gold nanospheres whose synthesis is well-controlled, with potentially less toxic effects, as well as to use nanosecond NIR lasers at ~1064 nm, whose penetration into tissues is much greater than visible wavelengths.

We discovered that irradiation of gold nanospheres in living organisms at relatively low pulse energies led to closer location of NPs in clusters and more profound red-shifting owing to the gentle laser removal of the biologically compatible coating from the NPs (e.g. polyethylene-glycol). In contrast, pulse energy with increased energy led to disintegration of the clusters owing to strong NP heating, bubble formation and even NP explosion (21,27). These effects can also lead to the movement of individual NPs with high speed from disintegrated nanoclusters. These gold laser-activated 'cassette nanobombs' may enhance cell killing through cell membrane damage by laser-induced 'gold nanobullets' (19).

The possibility of enhancing PT/PA contrasts in nanoclusters in living organisms also stimulated an idea for developing initial clustered NPs at moderate sizes of 30–60 nm consisting of shortened CNTs and their hybrids or 2–10 nm gold NPs, either bare (to enhance red-shifting) or coated with a thin layer of DNA or incorporated in viral capsids (Fig. 1B–D). Another example includes DNA-guided self-assembly of multilayered NP composites with controlled plasmonic properties (Fig. 1E) (22). Combination of multiple discrete nanoscale materials into a single nanostructure would be very useful in a variety of applications, including NP-based biomedical theranostics. This would allow the implementation of multiple tasks in parallel or in sequence and acquiring more comprehensive, accurate and reliable information in the same system using multiple modalities. Also the control over the structural configurations would lead to substantial functional enhancements by encouraging favorable interactions between individual nanocomponents, further enhancing the sensitivity and selectivity of the diagnostic modalities. Furthermore, multifunctional, specific and selective targeting can be achieved through selective and controllable incorporation of multiplex biocomponents (e.g. antibodies and DNA) to the system, assembled (22) by attaching probe DNAs or antibodies to the designated DNA sequence address. Recently, we demonstrated the possibility of tuning the

NPs' plasmonic properties through their controlled nanostructure assembly (43,44; unpublished result obtained in 2008–2009 in Kim's laboratory and presented as the preliminary data in the USDA/NRI grant ARK 02062, 'Engineering Ultrasensitive, Electrically Addressable Nanotube-Wire Sensors Through Controlled DNA-Nanotube Interfacing', and the NSF grant CMMI-0709121, 'Exploration of DNA-Based Nanoscale Building Block for Controllable and Scalable Fabrication of Active Nanostructures'). The self-assembled 1D, 2D and 3D gold NP nanocomposites showed considerably red-shifted plasmon resonances with appreciably enhanced absorbance in the NIR, owing to the plasmon coupling between NPs in the nanocomposites. This approach would provide new and versatile routes towards extending the capability of current NP-based PA/PT technology and enabling NIR-responsive, multifunctional, multiplexing and multimodal technology for noninvasive PA/PT cancer diagnosis and therapy with greater control.

3. THE PROPERTIES AND FEATURES OF CNTS

3.1. Optical properties of CNTs

Several techniques have been developed over the years to synthesize CNTs, each of which has been covered at length in separate reviews, including: high pressure carbon monoxide, chemical vapor deposition, arc discharge, and laser ablation (37–40). Having all its atoms exposed on the surface, a SWNT (Fig. 2A) has a very high surface area (~1300 m^2/g in theory), allowing efficient interaction between the SWNT and the optical radiation. SWNTs are characterized by a very broad and flat optical absorbance spectrum, spanning the UV, visible and NIR spectra (Fig. 2B). The vast majority of the photons that interact with the SWNT will be absorbed by it, leading to local heating around the vicinity of the SWNT (4,9,24). When the incident light is an intense nanosecond laser pulse, the local heating around the SWNT leads to the emission of an ultrasound wave, according to the PA effect (4–13,45). Semiconducting SWNTs with small band gaps on the order of 1 eV exhibit fluorescence properties with excitation and emission wavelengths in the NIR range. Importantly, different SWNT chiralities lead to different and characteristic excitation–emission wavelengths (46). While most of the light that interacts with the SWNTs is absorbed, a very small fraction of the photons will scatter inelastically, leading to distinctive Raman scattering spectrum. The unique Raman signature of SWNTs can then be used for detection and imaging *in vivo* (47–51). Similarly to SWNTs, MWNTs exhibit strong optical absorption characteristics, which make them potentially attractive PT and PA contrast agents (24). However, apart from pure optical absorption, they do not possess the rich optical characteristics of SWNTs.

3.2. Hybrid CNTs

3.2.1. Golden CNTs—Despite the excellent promise of CNTs as PA/PT contrast agents for biomedical applications, several questions remain regarding their safety and biocompatibility in humans (52–55). Furthermore, owing to the CNTs' relatively low NIR absorption coefficient compared with other nanoparticles, such as gold NPs (GNPs) (9,30,56), higher concentrations are generally required for effective PA/PT theranostics (8,9). To improve the CNTs' PT and PA effects, new types of hybrid GNPs consisting of an SWNT core surrounded by a gold layer were recently introduced (Fig. 2B) (9). The new

SWNT-mediated hybrid NPs combines the optical NIR absorbance of gold and CNTs and the biocompatibility and bioconjugation potential of gold to realize the advantages of both CNTs and GNPs. The synthesis process involves SWNTs and Au salts in water and does not require additional chemical reductants or catalysts agents. Two types of hybrid NPs were synthesized by tempering SWNTs' size and their aqueous dispersity. Hybrid rod-shaped Au-plated SWNTs (termed golden carbon nanotubes, GNTs) (9), with a thin layer of Au around the SWNT core, were synthesized using short (~100 nm) and well-dispersed SWNTs in water. When even shorter SWNTs (~30 nm) were used, monodisperse plasmonic hexagonal bipyramidal gold nanocrystals with well-defined size and shape resulted (57). The GNTs exhibited a unique set of features, in particular, enhanced NIR absorption contrasts. They showed two plasmon absorption maxima (Fig. 2B) in the visible region of 520–530 nm (similar to transverse absorption of Au nanospheres) and in the NIR region of 800–900 nm, similar to the longitudinal response of gold nanorods (GNRs). Their plasmon responses in the NIR were significantly higher (85- to 100-fold for GNTs; 25-to 30-fold for bipyradimal nanocrystals) than those of the SWNTs without the gold layer (Fig. 2B). This implies that potentially lower concentrations would be required for effective PA/PT diagnostic and therapeutic applications. The synergistic plasmonic effects of the gold shell and the potentially empty SWNT core were attributed to such highly enhanced NIR responsiveness. Their unique optical response with two absorbance maxima also suggests their potential as multi-color NPs for multiplexing studies of PA and PT nanodiagnostics and nanotherapeutics (8,9,11,25). Finally, recent *in vitro* and *in vivo* results indicated that the SWNT-Au hybrids have minimal cytotoxicity, as further described in later sections of this review.

3.2.2. Dye-enhanced CNTs—While the optical absorption spectrum of SWNTs is relatively flat across the visible and the NIR regimes, their spectrum can potentially be altered by adding additional dye molecules such as on the surface of the nanotubes (7). Taking advantage of the very high surface area per volume ratio of SWNTs, potentially many such small optical dyes can be attached to the surface of a single SWNT. As SWNTs have hydrophobic benzene ring structures on their surface, one may be able to stably load molecules onto the SWNTs through noncovalent pi–pi stacking bonds (65). Upon incubation of SWNTs with ICG, a strong and stable binding of ICG molecules to the surface of the SWNT occurs, leading to a ~20-fold increase in the optical absorption of the SWNT (Fig. 2C).

The quantitative reasoning behind this approach of dye-loaded SWNT lays in the unique relationship between the optical absorbance and the molecular weight of small optical dyes versus that of NPs (Table 1). While small optical dyes such as ICG have a lower optical absorption than SWNTs, they are also significantly smaller. The absorption coefficient of ICG divided by its molecular weight, however, is higher than that of SWNTs and significantly greater than that of gold-based NPs. This suggests that creating a carrier for small optical dyes, such as a SWNT, may be highly beneficial, as shown in Fig. 2(C).

Thus, while ICG exhibits 30 times and 5×10^3 times lower optical absorbances than SWNTs and GNRs, respectively, it is also 220 times and 45×10^6 times lighter than SWNTs and GNRs. Hence, on an absorbance-per-weight measure, ICG is ~7 times more efficient than

SWNT and ~9000 times more efficient than GNRs in absorbing light. It should be further noted that, unlike ICG and SWNTs, whose absorbance comprises only optical absorption, the optical absorbance of GNRs comprises both optical absorption and optical scattering, where the latter does not contribute to the PT/PA signal of the particle. Finally, it should be noted that, if volume is considered instead of molecular weight, GNR will be more efficiently absorbing than SWNTs. Hence, it is still not certain which parameter should be used for the comparison. In addition, ICG is photobleaching, a characteristic not experienced by most NPs, including SWNTs and GNRs.

3.3. Functionalization of CNTs and its hybrids

The importance of functionalization of NPs as molecular contrast agents cannot be overstressed, and has been reviewed in great detail before (79). In order to allow the contrast agents to reach a molecular target and thereby highlight it, the NPs need a biological moiety to act as a molecular linker to the target (in which case they are referred to as molecular imaging agents). This targeting moiety can be in the form of an antibody, peptide and other forms (61). Beyond the ability to bind to molecular targets, it is important to properly functionalize CNTs because raw CNTs have hydrophobic surfaces and are therefore not soluble in aqueous solutions such as blood. Proper functionalization of CNTs has been shown to be instrumental for preventing possible toxic effects of the CNTs, as further described in later sections of this review.

Surface functionalization of CNTs has been demonstrated with either covalent or noncovalent bonds. As CNTs are naturally inert, covalent functionalization typically involves creating defects on the sidewalls of the CNTs. To perform that, oxidation reactions with oxidizing agents such as nitric acid are most commonly used (62,63). These reactions were observed to create sp^3 carbon atoms on SWNTs, which were then used to further conjugate animo acids to the SWNTs (64). However, despite the fact that oxidized CNTs are soluble in water, they aggregate in the presence of salts owing to charge screening effects, which prevent their practical use *in vivo*. One solution for this has been to further attach hydrophilic polymers such as poly(ethylene glycol) (PEG), which resulted in CNTs that are highly stable in biological environments (65,66). Another common type of covalent bonding to CNTs is cycloaddition reaction (67–70). However, covalent bonds commonly interfere with the natural physical properties of the CNTs, including their Raman scattering and their photoluminescence, an effect that does not exist in noncovalent functionalization of CNTs. In noncovalent functionalization, the CNT surface is coated with amphiphilic surfactant molecules or polymers such that the hydrophobic surface of the CNT is noncovalently attached to the hydrophobic end of the surfactant. Multiple studies have utilized this pi–pi interaction to noncovalently bind the CNT surface to porphyrin (71) or pyrene (72–74), which later allowed for further functionalization of proteins on the CNT surface. Other noncovalent bonding included pi–pi stacking between the CNT surface and DNA (75), although there have been concerns regarding the serum stability of DNA-wrapped CNTs owing to potential enzyme activity that may degrade the DNA wrapping (76). Amphiphilic polysaccharides and their derivatives, such as starch (77) and dextran sulfate (78), have also been employed to enfold SWNTs, enhancing their biocompatibility and solubility in biological solutions and mitigating their potential toxicity. Polysaccharides have a higher

threshold for denaturation in the biological solutions, potentially rendering higher serum stability compared with DNA or proteins. The polysaccaride-coated biohybrid SWNTs hold promise for biological and biomedical applications owing to the synergistic unique properties of SWNTs and polysaccharides, such as enhanced NIR contrast, aqueous solubility and biocompatibility (78). Finally, PEGylated phospholipids (PL-PEG) were also used for noncovalent functionalization of SWNTs (59,65). These PL- PEG-SWNT exhibited very high water solubility and serum stability, owing to the two hydrocarbon chains of the lipids, which strongly bound to the SWNT surface. The PEG rendered water solubility and biocompatibility and allowed for further functionalization with targeting moieties (59). Further *in vivo* toxicity studies have shown that these PEGylated SWNTs exhibit no evident toxic effects in mice (82). For more exhaustive review on CNT functionalization, see a recent review article by Liu *et al*. (79).

Surface coating of CNTs with more biocompatible metal NPs, such as Au, was suggested as another approach to mitigating raw CNTs' intrinsic limitations, including aqueous solubility and toxicity. Recently, the unique size-dependent phenomenon of SWNTs has allowed the crafting of monodisperse Au-SWNT hybrids (GNTs) with different sizes and shapes (9,57). The GNTs can be easily conjugated to targeting moieties, such as antibodies and peptides, using basic thiol chemistry (80). Furthermore, the number and location of the functional groups on these hybrid GNPs can be controlled on the basis of the recently developed aqueous-phase solid-phase monofunctionalization methods (43,44). This would enable not only more controlled and stable functionalization of targeting moieties but also quantitative analyses by controlling the number of recognition units per NP.

3.4. Safety of CNTs and its hybrids

The safety of CNTs has been explored in numerous studies both *in vitro* as well as *in vivo*. The results of these studies varied significantly by the type of CNT as well as its functionalization. While well-functionalized CNTs with biocompatible surface coatings have been shown to be nontoxic *in vitro* to cells (73,81) and *in vivo* in mice (82), different CNT geometries, functionalized and particularly nonfunctionalized raw CNTs were shown to be toxic to cells (49,83–85) and to mice (86,87) and rats (88,89) upon inhalation and upon intra-abdominal administration (90). These studies and others have therefore led to the general understanding that the toxicity or safety of CNTs seems to be highly dependent on the geometry and surface functionalization of the CNTs.

In vitro, the toxicity of raw CNTs (i.e. without functionalization) has been investigated and found to be significant. It was found that raw SWNTs can inhibit HEK 293 cell proliferation (85) and that raw MWNTs induce cell cycle arrest and increase apoptosis/necrosis of human skin fibroblasts (84). Other studies have shown that using nonbiocompatible functionalization (91) or a too low density of functionalization (92) may also lead to toxic effects on cells. However, it was further shown that choosing the appropriate functionalization leads to no toxic effects on cells. For example, SWNTs PEGylated noncovalently through phospholipids were shown to be highly stable in serum while exhibiting no enhanced apoptosis or reduced proliferation in various cell types (31,93,100). Other types of CNT functionalizations were shown not to lead to toxic effects on cells,

including biomimetic coating (73,94,95), covalent functionalization with 1,3-dipolar cycloaddition (81,96), amphiphilic helical peptides (97), polysaccharides (77,78) and serum proteins (98). All in all, this suggests that CNTs with proper serum-stable functionalization show little to no toxicity, while raw CNTs or CNTs with minimal functionalization show highly toxic effects in cells.

In vivo, raw CNTs have shown obvious toxic effects on the pulmonary system when introduced intratracheally to animals (86–89). These results can be explained by the fact that these were raw CNTs, which are hydrophobic and therefore form aggregates that may get stuck in the lung airways. However, it is important to understand that these toxicity results cannot be generalized to other methods of delivery or to functionalized CNTs. Indeed, a preliminary toxicity study on PL-PEG_{5000} functionalized SWNT followed in 2007 and found no evident toxic effects in mice injected with the nanotubes intravenously at even high doses of 3 mg/kg over a period of 4 months (95). The blood pressure and blood counts of the mice were analyzed every month and at the end of the 4 month period, necropsy and tissue histology validated there were no evident toxic effects of the SWNTs. A follow-up toxicity study that looked at the biodistribution and secretion pathways of the SWNTs from the body also found no long-term toxic effects of the SWNTs when injected intravenously to living mice (83). Finally, SWNT that were functionalized differently using Tween-80 were found to have relatively low toxic effects at very high doses (~40 mg/kg) (99).

For the hybrid Au-SWNTs, no apparent adverse toxicity effects were observed according to the preliminary *in vitro* cell viability and proliferation assays as well as an *in vivo* study of their impact on mouse vasculature over 1 month (9). However, conflicting data have been reported on the toxicity of GNPs (101–106). The possible hazard of nanomaterials represents a potential obstacle for their application to nanomedicine; thus, a full-scale systematic investigation of the toxicity of GNPs is required before human applications can be employed. Nonetheless, the GNTs have a high potential to improve the biocompatibility of CNTs, for both their potentially minimal toxicity and to the fact that much lower concentrations are needed, compared with plain SWNTs, owing to their high NIR PA/PT response. A recent approval for a pegylated colloidal gold nanoparticle (CYT-6091) to proceed to phase I clinical trials to target solid tumors in humans brings promise that such Au-SWNTs will also translate to humans in the future.

4. APPLICATION OF CNT AND ITS HYBRID

4.1. *In vivo* PA molecular imaging of tumor angiogenesis using SWNT-RGD

Recently, SWNTs conjugated with RGD peptide through PL-PEG_{5400} were demonstrated to target $\alpha_v\beta_3$ in tumors, a vascular integrin associated with tumor angiogenesis (59). By radiolabeling the SWNTs with ^{64}Cu, the tumor accumulation was quantified as ~14 %ID/g (percent injected dose per gram) (59), while control untargeted SWNTs without the RGD peptide showed significantly lower accumulation of ~3 %ID/g.

This first demonstration of molecular targeting of SWNTs in living subjects led to multiple imaging studies utilizing various physical properties of SWNTs, including Raman scattering (48,50) and PA imaging (6,7). While Raman imaging of the CNTs takes advantage of the

characteristic Raman spectrum of sp^2 carbon materials (G-band at 1582 cm^{-1}), PA imaging takes advantage of the near-infrared light absorption characteristic of CNTs.

SWNT-RGD have been extensively characterized both *in vitro* and *in vivo* by rigorously following the required validation experiments for a new imaging agent, as listed in Table 2 (6). This included testing the PA signal stability when introduced to serum, cell uptake and photobleaching, and characterizing the signal–concentration curve. However, perhaps of most importance were the *in vivo* sensitivity and *in vivo* targeting tests. The sensitivity in living mice was quantified and found to be 50 nM (i.e. 50 nM of SWNT-RGD gave the equivalent PA signal as the background tissue signal; Fig. 3). Furthermore, mice bearing U87 glioblastoma xenograft tumors injected with SWNT-RGD showed significantly higher PA signal in the tumor as compared with mice injected with untargeted SWNTs (Fig. 4). Finally, Raman spectroscopic imaging was used to validate the accumulation of SWNT-RGD and the lack of accumulation of control untargeted SWNT in tumors *ex vivo*.

4.2. ICG-enhanced SWNT-RGD for *in vivo* PA molecular imaging of tumor angiogenesis

Despite the fact that SWNT-RGD has favorable biodistribution and exhibit high tumor accumulation, one cannot assume that the ICG-modified SWNT-RGD will behave similarly (7). The shape of SWNT-RGD is similar to that of SWNT-ICG-RGD, particularly owing to the fact that ICG is attached to the surface of the SWNT, while PEG-RGD extends further away from the SWNT (Fig. 2C). However, the two NPs may have significantly different molecular weights, charge and ζ-potential, and therefore, potentially different biodistributions. Hence, in order to validate that SWNT-ICG-RGD can also be used as a PA imaging agent, one has to study the particle the tests listed in Table 2 (7). *In vitro* testing of the SWNT-ICG-RGD contrast agents showed that they are highly stable in serum; however, unlike plain SWNT-RGD, some degree of photobleaching was observed to the extent of ~30% over 1 h of strong nanosecond-pulsed laser illumination. Despite the fact that SWNT are highly resistive to photobleaching, small molecule optical dyes, such as ICG, are more susceptible to photobleaching and, hence, this observed photobleaching is probably due to photobleaching of the ICG molecules. The sensitivity of ICG- modified SWNT-RGD in living mice has been estimated to be 170 pM (Fig. 5). This represents a significant improvement in sensitivity of over 300-fold as compared with plain SWNT-RGD. This improvement in sensitivity is primarily due to the higher optical absorption of the new NPs, as well as the ability to shift the laser excitation wavelength from 690 to 780 nm (the absorption spectrum maximum of SWNT-ICG-RGD), at which the background tissue absorption is significantly reduced. Finally, in a similar experiment to that previously described for SWNT-RGD, SWNT-ICG-RGD has been shown to specifically target the $\alpha_v\beta_3$ integrin in living tumor-bearing mice (7).

4.3. PA-PT molecular theranostics of lymph vessels and sentinel lymph nodes

Golden nanotubes (GNTs) conjugated with an antibody specific to the lymphatic endothelial hyaluronan receptor-1 (LYVE-1) were used for PA/PT mapping of lymphatic endothelial cells in mouse mesentery (Fig. 6A) (9). The LYVE-1 receptor is one of the most widely used lymphatic markers of endothelial cells and their expression and functional activity are closely correlated with the regulation of cell migration, metastasis, inflammation and other

important processes (9). The PA/PT mapping of nude mouse mesentery within the field of interest (Fig. 6B) was obtained by an automatic scanning microscopic stage and PA and pump-probe PT thermal lens detection schematics with a focused laser beam (optical parametric oscillator, OPO, 410–2600 nm, 8 ns, 2–10 μm in diameter). The administration of the bioconjugated GNTs led to the appearance of strong PT and PA signals, which significantly exceeded those from endogenous backgrounds and were preferentially located in the lymphatic walls (Fig. 6C). The PA/PT mapping at 15 min after unconjugated GNT administration revealed randomly scattered fluctuating signals in lymphatic flow above the background; however, no signals were observed in the lymphatic walls. Within 1 h, signals became diminished in lymphatics owing to their natural washing by the lymph flow. These findings strongly suggest PA molecular targeting of LYVE-1 receptors, which showed very heterogeneous distribution along the vessel walls. These signals were highly stable during the 1–2 h of observation. An increase in the laser fluence from 35 to 80 mJ/cm^2 led to highly localized (within 5–10 μm around absorbing centers) microbubble-related damage to the lymphatic wall without notable changes in surrounding tissue (Fig. 6D).

In addition, PA detection and PT ablation of GNT-labeled tumor cells in SLNs as the first metastatic places for disseminated cells from primary tumors was proposed (9) Supplementary; (11). To verify this approach, around 100 tumor cells were directly injected into SLN of nude mice. Then, the GNT–folate conjugates were injected in mouse ear followed by PA continuous monitoring of SLN using their transcutaneous laser irradiation (20 mJ/cm^2; 850 nm). Five minutes after the injection of the conjugated GNTs, strong PA signals above the background with contrast of 10–15 appeared in the SLN, probably owing to their delivery through the lymph vessels to the SLN and the targeting of individual tumor cells. Subsequent application of one-pulse NIR laser with fluence of 100 mJ/cm^2 led to a decrease of these strong signals to background level, suggesting laser-induced eradication of tumor cells. However, when the experiment was repeated with unconjugated GNTs, low PA signals with contrast of ~3 above the background was observed on the injection spot of tumor cells, suggesting random distribution of GNTs in the SLN volume. To verify this data, *ex vivo* experiments mimicking the lymph node micrometastsis were carried out using lymph nodes excised from mice (Fig. 7A). Breast tumor cells dual labeled with GNT-folates and fluorescein isothiocyanate (FITC) were injected into the excised lymph node. PA signals (Fig. 7B) were recorded exclusively from the fluorescent cells, verifying that the GNT-bound tumor cells are the source of PA signals. The irradiation of fluorescent cells with one laser pulse at relatively high laser fluence (100 mJ/cm^2) led to the disappearance of the fluorescence signal and substantial decrease in PA signals to background level (Fig. 7C). This suggests that the cells disintegrated through laser-induced microbubble formation around overheated GNTs. The strong localization of the damaged area was validated by optical imaging (Fig. 7C). The results of the *in vivo* and *ex vivo* studies support the feasibility of the PA/PT technique using GNTs as PA/PT contrast agents for the *in vivo* detection and killing of metastatic cells in SLNs.

4.4. *In vivo* real-time two-wavelength PA detection of three cell types in lymph flow with multicolor nanoparticles (*in vivo* lymph flow cytometry)

Because of the relatively short (10^{-2} to 10^{-3} s) time during which cells in the lymph flow appear in the detected volume, existing time-consuming imaging and spectral scanning methods are not quite adequate for *in vivo* multicolor PAFC (4). Therefore, a novel approach for real-time multispectral exposure of fast-moving cells labeled with multicolor probes was introduced and experimentally proven using two-wavelength modes and three nanoparticle types (5). Necrotic and apoptotic lymphocytes and live neutrophils were labeled with GNRs, gold nanoshells (GNSs) and CNTs, respectively. The GNSs and GNRs had relatively narrow absorption bands, 180 and 75 nm with maximum absorption at 860 nm and 640 nm, respectively; in contrast, the absorption spectrum of CNTs was relatively broad, covering the visible and NIR range. These labeled cells, mixed in equal proportions, were injected into a rat tail vein. After 6 h, in mesenteric lymphatics irradiated with two OPO laser pulses at wavelengths of 865 nm (8 ns) and 639 nm (12 ns) with a 10 μs delay between the pulses at pulse rate of 50 Hz, rare (0.5–3 per min) PA signals associated with cells labeled by different NPs were observed. In particular, very rare PA signals from necrotic lymphocytes were generated by a laser pulse at 639 nm only after a 10 μs delay (Fig. 8), while PA signals from apoptotic lymphocytes were generated by a laser pulse at a wavelength of 865 nm with no delay between the pulses. Live neutrophils yielded two PA signals with a 10 μs delay because of CNT absorption at both 639 and 865 nm wavelengths. The time-resolved mode was found to allow the identification of multicolored NPs with partly overlapping absorption spectra by a comparison of the PA signal amplitude ratios at different wavelengths.

4.5. *In vivo* multiplex targeting and two-color detection of circulating tumor cells in blood flow

About 90% of cancer deaths result from metastatic spread from the primary tumor. Detection of circulating tumor cells (CTCs) is therefore a marker of metastasis development and therapy efficiency (see references (5),(8) and (32), and their citations). However, as the sensitivity of most existing CTC assays is fairly limited as they rely on 5–10 ml of patient blood volume, incurable metastases may already have developed by the time of initial diagnosis of the CTCs. As we previously demonstrated, the sensitivity can be improved by assessments of a significantly larger blood volume *in vivo*, potentially the entire patient blood volume(~5 l in adults) (4,8,25,32). Because most CTCs exhibit a very low endogenous PA signal (except some melanoma cancers), NP labeling has been applied for detection of CTCs (4). Since human tumor cells are heterogeneous and not all tumor cells express one given biomarker, a multiplex targeting strategy was applied to increase specificity of *in vivo* CTC detection (8). Simultaneous targeting of the urokinase plasminogen activator (ATF) and folate receptors (Fig. 9A), both of which are highly expressed (70–92%) in human breast tumors but not expressed by normal blood cells, was performed using two conjugated NPs: magnetic (MNPs) and GNTs with absorption spectra in NIR region (Fig. 9B), allowing two-color detection at laser wavelengths of 639 and 900 nm. The best targeting efficiency of cancer cells (~96%) was observed *in vitro* with the NP cocktail during 30 min labeling under static and 5–10 min under flow condition at a velocity of 0.5 cm/s. The optimal NP concentration and solution volume were estimated to be 10^9

NPs/ml (for GNTs) and 10–20 μl, respectively, which did not yield detectable PA signals above blood background in mouse ear microvessels after intravenous injection. This suggests that there was a negligible level of PA signals from unbound or nonspecifically bound NPs. To detect CTCs originating from a primary tumor, 10^6 of MDA-MB-231 cells were inoculated subcutaneously to nude mice. At 2, 3 and 4 weeks of tumor development, the optimal cocktail of conjugated NPs was injected via the mice tail vein. Photoacoustic flow cytometry (PAFC) started at 30 min post-injection to allow the clearance of most unbound NPs, and revealed a gradual increase in CTC counts at 2, 3, and 4 weeks, which roughly correlated with tumor progression (Fig. 9C). The capability of PAFC technology with GNTs was also demonstrated for molecular detection *in vivo* of circulating rare (1–3%) CTCs, namely cancer stem or tumor initiating cells, which could be responsible for metastasis progression and resistance to therapy (25). This clinically relevant technology, called the *in vivo* blood cancer test, has potential for the early PA diagnosis of primary tumor, cancer recurrence, monitoring of therapy efficacy and potentially even inhibition and prevention of metastasis by well-timed PT therapy, as previously demonstrated for melanoma (32).

4.6. *In vivo* studies of pharmokinetics of CNTs with high pulse rate fiber 1064 nm laser

The rapid growth of nanomedicine applications has placed demands on evaluation of pharmacokinetics of NPs (e.g. clearance rate and organ biodistribution). The pharmacokinetics of CNTs is highly dependent upon CNTs' type and size, their surface chemistry and their functionalized bio-targeting ligands according to the studies using different techniques. Intravenous administration of radiolabeled SWNTs functionalized with diethylene triamine pentaacetic acid and labeled with indium (^{111}In) in mice showed fast urinal clearance of CNTs and minimal uptake by the reticuloendothelial system, including the liver and the spleen, with a half-life of 3 h (107,108). However, other studies with radiolabeled CNTs in mice showed high and persistent CNT uptake by the liver and the spleen with slow and minimal urinal excretion, using ^{14}C-taurine functionalized CNTs (109,110) and 1,3-dipolar cycloaddition (110). Using SWNTs' Raman spectroscopic signatures, intravenously administered PEGylated SWNTs were shown to have blood circulation up to 1 h, relatively low uptake by the liver and the spleen, and near-complete clearance from the main body organs in ~2 months, without apparent toxicity (49). A branched PEG structure enabled longer blood circulation half-life by offering a more effective coating on the SWNT surface (e.g. 5 h for a branched PEG compared with ~2 h for a linear PEG with a molecular weight of 7 kDa) (49). Also covalently PEGlyated SWNTs yielded an even longer blood circulation half-life of ~22 h (111).

As CNTs have an intrinsic absorption in the visible and NIR spectral ranges, PAFC is an ideal tool for real-time label-free time- resolved monitoring of CNT pharmacokinetics in the blood using a limited number of animals (4,8,18). An advanced ultra-fast PAFC was applied with a high-pulse-rate (up to 0.7 MHz) 1064 nm fiber laser for this purpose (18). Figure 10(A) shows that the PA signals from skin with blood vessel are of the same amplitude at 1064 nm as signals acquired in the 850–900 nm range (2). This suggests that a laser operating at 1064 nm is an excellent optical source for PAFC, providing low background signal from tissues. The traces of bare CNTs (Fig. 10B) showed both an increase in the

baseline level, attributed to the presence of individual CNTs in the detected volume, and strong fluctuations above of baseline, probably associated with CNT aggregates as previously observed (4). The clearance rate of CNTs was in the range of 20–30 min, although rare signals were seen over a few hours and even 2–3 days. Thus, time-resolved PAFC with high pulse rate lasers should also be useful for the evaluation of clearance of NPs, and the parameters which may interfere with their clearance, including the protective materials, the NP coating and the presence and formation of aggregates in blood circulation. PAFC has also been applied to study the clearance rate of ICG (112), lymphuzurin (4), GNRs (4,112), MNPs (8) and GNTs (8,9).

4.7. *In vivo* real-time counting of circulating individual bacteria labeled with CNTs

Despite major advances in medicine in the last decade, microbiologically based diseases continue to present enormous global health problems, especially owing to the appearance of multidrug-resistant bacteria strains. The critical steps in the development of bacterial infections include their penetration into the blood and lymphatic systems, their interactions with blood cells in flow or with endothelial cells, and their toxin translocations in the host organisms. Unfortunately, little is known about bacteria circulation in the blood pool, their clearance and adherence rates, and other kinetic parameters, which might be very important for understanding the transition from the bacteremic stage to the tissue invasion stage.

The capability of PAFC of monitoring circulating individual *S. aureus* and *E. coli* labeled with CNTs in blood flow was estimated on the mouse ear model (4). The incubation of *S. aureus* with CNTs was performed for 30 min at 37 °C without antibodies to avoid the potential influence of immunogenicity on bacteria circulation. After intravenous injection of CNT-labeled bacteria in 100 μl suspension and concentration of 5×10^5 bacteria per ml into the mouse's circulatory system through the tail vein, we observed the rapid appearance of bacteria in the ear blood microvessels, followed by their elimination from the blood circulation after approximately 5–7 min (Fig. 11) with the appearance of rare PA signals for more than 2 days. The high sensitivity of the PA technique allowed both *in vivo* and *ex vivo* detections of the presence of labeled bacteria in the tissue surrounding the examined blood vessels and in the liver by a spatial scanning focused laser beam (i.e. scanning PA microscopy (123)), demonstrating the first application of PA mapping technique for histology with no sample preparation (Fig. 15) (4,5). Thus, the ultrasensitive, rapid PA detection of infection at a single bacterium level may supplement or replace conventional assays, for example, the time-consuming polymerase chain reaction (PCR) and others that are only currently available *in vitro*. It is estimated that the described PAFC has the potential to detect just a few bacteria in a whole mouse blood pool during continuous PA monitoring in the relatively large vessels in approximately 1 h. PAFC with high pulse repetition rate lasers also provides time-of-flight monitoring of the velocity of individual cells, bacteria and nano- and microparticles *in vivo* through measuring the PA signal widths, as previously demonstrated for CTCs and CNTs (18,32).

4.8. PA-PT theranostics with transient and stationary nano- and microbubbles

4.8.1. Laser-activated transient bubbles as therapeutic PT contrast agents—In 2003, we introduced pulsed PT nanotherapy (also termed selective nanophotothermolysis)

for killing individual cancer cells and bacteria targeted by strongly absorbing NPs (19,22–24,115,116). The killing mechanism was related to the formation of nano- and microbubbles around laser-overheated NPs, which during expansion mechanically damaged cellular structures. To enhance the therapeutic effects, we proposed a mode in which nanobubbles from individual NPs or their clusters spatially coalesce, thus producing more powerful synergistic effects on biological structures (20–24,33,34). Recently, we extended this approach by generating periodic temporally overlapped microbubbles using a high pulse repetition rate laser in the MHz range (18). This mode, instead of the previously used single exposure and singe transient microbubbles, used periodic multiple microbubbles as new theranostic agents both for laser and ultrasound diagnosis and therapy.

In addition to the treatment of cancer cells, we demonstrated the first application of this technology for nanophotothermolysis of *E. coli* labeled with CNTs (24). The pre-treated SWNTs and MWNTs spontaneously self-assembled as clusters on bacteria surfaces (Fig. 12) without any bioconjugation steps or targeting moieties. *In vitro* studies revealed that notable changes in bacteria viability (~80% cell death) were observed after ~50 NIR laser pulses at 1064 nm at a relatively low fluence of 0.3–0.5 J/cm^2 with complete bacteria disintegration with slightly higher fluences. After intravenous injections of bacteria-labeled CNTs to mice, the NIR PAFC could effectively detect CNT-labeled *E. coli* in the blood at laser fluences of 20 mJ/cm^2 at 850 nm, which is much less than the damage threshold of red blood cells. Furthermore, multiple laser exposures at 50–100 mJ/cm^2 yielded a gradual decrease in PA signal amplitude, leading to thermal and bubble-related disintegration of CNT-labeled bacteria. These studies indicated the likely potential of CNTs as PA/PT molecular contrast agents for antimicrobial theranostics that can be self- delivered to the infected area, spontaneously adsorbed to infectious pathogenic bacteria and to self-assembled clusters. Additional applications include the NIR response not only for PA/PT diagnostics (at low laser fluences) to detect and monitor bacterial infections, but also for PT therapy to selectively kill the disease-causing pathogens without harmful effects for surrounding tissues. The unique properties of CNTs, in particular NIR contrast and the ability to adhere to various bacteria (24,121), would be beneficial to not only the antimicrobial theranostics but also other applications that require bacterial removal, such as water treatment, food processing and more.

4.8.2. *In vivo* detection of circulating microbubbles conjugated with CNTs for selective nanothrombolysis—During our experiments, we observed bubble cavitation at least a few cycles after a single laser pulse and even the formation of stationary 1–10 μm microbubbles filled with air as a product of laser ablation. In addition, we discovered that the accidental presence of small air microbubbles attached to cell membrane with NPs (e.g. after laser exposure or after preparation procedures) facilitated PT bubble generation with lower thresholds compared with NPs alone. These phenomena are probably explained by the decrease in nucleation threshold because less energy is required for nucleation and thus more energy has been transformed to the expansion of already existing bubbles. Moreover, the level of laser energy required to produce the bubbles around CNTs (24), GNTs (9) and quantum dots (34) was significantly decreased (5- to 15-fold) by adding ethanol to the medium around the NPs because of its superior thermodynamic parameters compared with

water (lower boiling point, heat capacity, heat required for vaporization, higher coefficient of thermal expansion and lower surface tension) (24). With advanced NPs such as GNTs and GNSs, we eventually demonstrated an extremely low threshold for bubble formation in water at the level of 5–10 mJ/cm^2 and in ethanol at 0.9 mJ/cm^2 (9,122).

Based on these discoveries, we developed NPs with enhanced PT/PA contrast properties using external layer saturated with ethanol (or other liquids) or integration of NPs with FDA-approved ultrasound contrast agent: 0.5–2 μm microbubbles (Fig. 13A), marketed as Definity (lipid membrane filled with perflutren gas) from ImaRX (unpublished results obtained in 2007 in Zharov's laboratory and presented as the preliminary data in the NIH grant 1RC1CA1464919). Microbubbles were prepared according to the standard manufacturer's procedure with slight modifications by adding absorbing agents (e.g. ICG, CNTs, GNS, MNPs, and GNRs) in various concentrations and with various coatings at the final stage of the synthesis. Labeling efficiency was controlled through increased linear (i.e. low laser energy) PT/PA signals from microbubbles with absorbing agents. These signals were significantly higher (10- to 50-fold) than the background signals of the surrounding water, (which themselves were likely due to some small and non-specific release of aborbing agents from the microbubbles to the surrounding water). (Fig. 13B). With PT and PA methods, we observed laser-induced bubble oscillation with a period range of 0.3–2 MHz. At an optimal agent concentration, microbubbles were relatively stable as intact microbubbles, while at higher concentrations, especially for CNTs, microbubbles were degraded, probably owing to enhanced gas leakage through agent- induced pores in the lipid layer. For intact microbubbles, threshold laser-induced evaporation at 850 nm was in the range of 2–8 J/cm^2, while the presence CNTs reduced this threshold to 10–30 mJ/cm^2 compared with 100–200 mJ/cm^2 for CNTs in water at similar concentrations. Gradual increase of laser energy above evaporation threshold led to sudden nonlinear (10- to 30-fold) amplification of both PT and PA signals compared with NP solution alone (Fig. 13C), accompanied by microbubble degradation at high laser energies. For GNSs and GNRs, the threshold evaporations were several times lower owing to their stronger absorption (this topic is beyond the scope of this review), while CNTs showed better targeting efficiency. After intravenous injection of 100 μl microbubble solution in concentration range of 10^{10}–10^{11}/ml to a mouse circulatory system, PAFC revealed the quick appearance of many microbubbles with typical clearance rates of 3–6 min (Fig. 13D). In the developed model of mouse thrombosis guided by high-speed imaging (up to 10 000 frames per second) (119), thrombi with microbubbles were visualized *in vitro* and *in vivo* in blood vessels (Fig. 13-F). Laser irradiation of microbubbles and thrombi *in vitro* and *in vivo* with therapeutically safe doses (~50–100 mJ/cm^2 at 1064 nm) led to the disappearance of both microbubbles and thrombi, suggesting effective destruction of thrombi as they were further taken away by the blood flow. Although we have checked the safety of this highly localized PT therapy for normal blood cells surrounding CTCs with laser-induced microbubbles (8,32) this issue requires additional study for new stationary microbubble–NP conjugates as PT/PA contrast agents. Microbubbles loaded with MNPs were captured by magnetic field in mouse circulation using a previously described method (8).

After further optimizations, nano- and microbubbles loaded with absorbing agents can be used for imaging (114) (S. Emelyanov reported a similar approach of contrast enhancement through evaporation at the 2011 BIOS Symposium) and for selective nanothrombolysis alone or in combination with theranostic ultrasound (113). Laser radiation can be delivered through an optical fiber under PAFC guidance, as we demonstrated previously for the detection and killing of metastatic cells (32).

4.9. Multimodal genetic-PT/PA analysis of CNT–plant interaction

Understanding the nature of interactions between engineered nanomaterials and plants is very important to comprehend the impact of nanotechnology on the environment and agriculture. However, to date, little progress has been made in studying nanoparticle–plant interactions at the single nanoparticle and genetic levels. Recently, using an advanced platform integrating genetic, PT and PA methods, a collaborative team in biomedical engineering, genetics and nanotechnology demonstrated (17) that CNTs added to growth medium may lead to: (1) transportation of CNTs in tomato plants through the roots to leaves and even to the fruits (Fig. 14); (2) growth enhancement of tomato plants; and (3) induction of previously unknown changes in gene expression in tomato leaves and roots, particularly up-regulation of genes, including those induced by pathogens. In this work, laser-induced nanobubbles around CNTs were used for amplification of PA/PT signals. In addition, spectral burning technique was introduced to remove undesired absorption background in PT/PA imaging (see below).

4.10. PT multispectral image cytometry of histological samples

There is a rapidly growing interest in the advanced analysis of histological data and the development of appropriate detection technologies particularly for the mapping of NP tissue distributions for nanomedicine applications. The capability of PA and PT scanning cytometry was evaluated for color-coded imaging, spectral identification and quantitative detection of CNTs and melanoma cells in histological samples with and without conventional staining (16). Using this tool and laser-induced nanobubble-based signal amplification, individual CNTs were identified in unstained lung and liver tissues 4 weeks after intravenous injection of the CNTs (Fig. 15). Comparison of PT and PA cytometry revealed that these methods supplement each other with a sensitivity advantage (up to 10- to 30-fold) in contactless PT technique in assessment of thin (≤100 μm) histological samples, while PA imaging provides characterization of thicker samples, which, however, requires an acoustic contact with transducers. An integrated high-speed PT/PA cytometry has the potential to provide histological analysis and immunohistochemistry of both intact and stained samples with high sensitivity at the zeptomolar concentration level.

4.11. PA and PT Raman spectroscopy of CNTs

Because CNTs provide strong Raman signals (47–50), a time-resolved Raman spectroscopy allowed *in vivo* real-time detection of CNTs or cancer cells labeled with CNTs in the lymph, blood and tissues of live animals with fast spectral acquisition times down to few milliseconds (51). The high sensitivity of PA and PT methods provided detection of Raman-induced thermal and acoustic signals in samples with Raman-active vibrational modes that

allowed individual cells to be imaged *in vivo* for the first time (15). In this study, two-frequency, spatially and temporally overlapping pump-Stokes excitation in counter-propagating geometry was provided by a nanosecond tunable (420–2300 nm) OPO and a Raman shifter (639 nm) pumped by a double-pulsed Q-switched Nd–YAG laser using microscopic and fiber optic delivery of laser radiation. The influence of background linear absorption was excluded by subtracting the nonlinear signal from linear signal components at different delay times between the pump and Stokes beams. The CNTs were identified through characteristic bands near 1593 cm^{-1} in PT/PA Raman spectra. The advantage of PT/PA Raman technique for spectroscopy, imaging, and cytometry with direct monitoring of the amount of heat deposited into the sample is much higher sensitivity compared with normal Raman spectroscopy, simpler optical setup and nanosecond lasers with lower requirements of phase matching and energy stability compared with coherent anti-Stokes Raman scattering (CARS) spectroscopy with picosecond and femtosecond lasers. The sensitivity of the PT/PA Raman technique can be further increased through laser activation of nano- and microbubbles around CNTs as a PA/PT signal amplifier (15). Indeed, if the temperature of the heated zone in linear mode (e.g. when the pump and Stokes laser pulses are not temporally overlapped) is close to the boiling point of water, even small additional Raman-related energy depositions (at 0 delay time) may increase the temperature slightly above the evaporation threshold, which is accompanied by sudden bubble formation leading to significant (10- to 50-fold) PT and PA signal enhancement.

The integration of linear and nonlinear PA and PT Raman techniques has the potential to enhance the chemical specificity and sensitivity to study lymph and blood biochemistry, circulating nano- and microparticles (e.g. chylomicrons), tumor, bones and fat distribution at the single-cell level (15,115).

4.12. Ultrasharp rainbow nanoparticles below the spectral limits for multicolor PA diagnosis and multiplex PT therapy

Spectral specificity of multispectral PA diagnosis and PT therapy may be limited by relatively broad absorption bands of PT/PA contrast agents (33). This problem can be overcome by using high-spectral-resolution nonlinear PT and PA spectroscopy. If the laser wavelength is away from the absorption centers, and the laser-induced temperature is slightly below the threshold for nonlinear effects (e.g. bubble formation), linear signals are generated. However, a shift in the laser wavelength toward the absorption centers will lead to an increase in energy absorption, and hence in the temperature of the absorbing zone. A temperature slightly above the evaporation threshold induces sudden nanobubble formation accompanied by nonlinear signal amplification. As a result, spectrally dependent signal amplification will lead to the sharpening of PT/PA resonances near the centers of the absorption peaks. To provide sharpening of the absorption dip, laser energy must be close to the threshold in the center of the dip. This will lead to spectrally dependent signal amplification if the laser wavelength shifts away from the dip's center, which is accompanied by an increase absorbed energy, and a profound bubble will be formed. New nonlinear spectroscopy demonstrated ultrasharp resonances up to a few nanometers wide (4–10 nm) embedded in the broad plasmonic spectra of gold-based nanoparticles, in particular in GNTs (33). It also demonstrated the narrowing of absorption spectra of conventional dyes

and cellular chromophores. This technique, in combination with contrast agents with low nonlinear bubble formation thresholds (0.9–5 mJ/cm^2) (9,122) can permit the study of nonlinear plasmonics at a level of spectral resolution beyond the spectral limits, measurements of tiny red and blue resonances in plasmonic nanosensors, and optimized multiplex PT/PA theranostics with 10–15 nonoverlapping colors that cannot be achieved with existing techniques.

4.13. Integration of PT/PA and spectral burning technique

Spectral hole-burning technique using phototransformation of molecules under a narrow-band resonant laser is a powerful tool for studying tiny structures in multiple inhomogeneously broadened absorption bands (120); however, its application for PT/PA spectroscopy has not been previously reported. Recently, this approach was successfully demonstrated for increased contrast of CNTs and other absorbing agents by selective PT erasing of undesirable absorption background in histological samples (16) and tomato plants (17), and spectral hole burning in a mixture of NPs with overlapping absorption spectra with simultaneous nonlinear spectral hole sharpening (33). In these applications, PT/PA methods provide a significant increase in the sensitivity and resolution of the spectral hole-burning technique.

4.14. *In vivo* PA blood and lymph tests

Diagnosis of many diseases begins with a common medical procedure: examination of a patient's blood sample, which is invasively drawn, usually from a cubital vein or finger tip. The analyses include the counting of blood cells, plasma proteins and many other biomarkers. However, the current biomarker repertoire often cannot detect treatable early-stage disease because the sensitivity of existing blood tests is limited by the small blood volume extracted (typically a few milliliters), in which theoretically no less than one abnormal cell or biomarker can be detected. As a result, the existing tests can miss up to 10^3 abnormal cells (e.g. tumor, or infections), in the entire blood volume (~5 l in an adult), which is sufficient for rapid development of disease to a stage that is barely treatable or is incurable (i.e. metastasis or septic shock).

To overcome these problems, in 2007 Zharov's team proposed *in vivo* blood and lymph tests on the basis of *in vivo* multispectral PAFC platform using low-toxicity ultrasharp rainbow NPs for targeting and identification of multiple disease-associated circulating multiple markers, abnormal cells or abnormal counts of normal blood cells (8,9,33,124,125). The possibility of developing a PA diagnostic device capable of examining a much larger volume of blood *in vivo* compared with conventional samples *ex vivo* is based on the well-established physiological fact that almost the complete volume of blood in a human adult passes through peripheral blood vessels with diameters of 2–3 mm within 1 h. In a larger vessel, such as the jugular vein or carotid artery (10–15-mm diameter), total circulation time is much shorter, just 5–10 min, with a flow rate of up to 10^9 cells/s (i.e. at least 10^3-fold faster than flow cytometry *in vitro*). The expected threshold of sensitivity of the assembled device is one cell of interest (or other biomarkers) in 0.1–1 l of blood (~10^2- to 10^3-fold more sensitive than existing assays). This could shift paradigms of the clinical roles of blood tests from disease staging and therapy efficiency to early disease diagnosis – hypothetically

before disease progression. Therefore, application of a well-timed, more effective, personalized therapy guided by PAFC real-time abnormal cell counting would be feasible. This new *in vivo* blood test can be used for the earliest diagnosis of cardiovascular and immune disorders, antibiotic-resistant bacterial infections, malaria, viral infections and AIDS. Many standard blood parameters currently measured by conventional *in vitro* blood testing can be also measured *in vivo* in real time more rapidly (a few minutes vs many hours) and with higher sensitivity.

4.15. *In vivo* photocoustic bone flow cytometry

Recently Zharov's team developed *in vivo* PA bone flow cytometry (Fig. 16A) for real-time detection of circulating normal cells (e.g. stem or immune), abnormal cells (e.g. CTCs or infection-related cells) and NPs in bones (unpublished result obtained in 2009 in Zharov's laboratory and presented as the preliminary data in the Department of Defense grant W81XWH–11–1–0123 'In vivo, noninvasive, ultrasensitive photoacoustic detection of early breast cancer metastasis in bones'). The bones are relatively transparent to NIR and ultrasound radiation. As a result, laser radiation, even after significant attenuation, may generate readable PA signals from strongly absorbing circulating NPs or cells targeted by NPs inside bones. In a study similar to the one described above, we used fiber delivery laser radiation for noninvasive irradiation of skin above a mouse tibia near a site where blood vessels enter the bone. Intravenous injection of CNTs (2 mg/ml, 50 μl solution) in a mouse tail vein led to the appearance of PA signal traces (Fig. 16B). Compared with monitoring CNTs in the ear and abdominal blood vessels (Fig. 10), in bone, PA signals were rarer with lower amplitude, and required increased laser energy (300–500 mJ/cm^2). To exclude possible background PA signals from CNTs circulating in blood vessels between fiber and bones, the fiber was gently attached to the skin in an area with no visible vessels and time-resolved detection of PA signal was used to select signals from cells in relatively deeply located bone. We also applied a minimally invasive approach by attaching the fiber on a tiny needle directly onto the bone surface. Scanning of the laser beam along the bone revealed rare stationary PA signals associated with the accumulated CNTs in bone. Similar results were obtained for pigmented melanoma cells and breast cancer cells (MDA-MD-321) targeted by gold nanorods. We believe that this clinically relevant technique after further optimization has potential for early, painless diagnosis of bone metastasis (noninvasive bone marrow biopsy) and cancer recurrence, and evaluation of therapy efficacy by the administration of strongly absorbing NPs functionalized to specific cancer cell markers, which are typically not expressed in blood and bone niches. In analogy to the detection of metastasis in SLNs (11), healthy bones produce low-level background PA signals because low concentrations of NPs are randomly and nonspecifically distributed in the bone tissue compared with a high local concentration of NPs in the targeted bone metastasis.

5. CONCLUSION

In this review, we have focused on the analysis of our recent results in the application of CNTs and their new hybrids with enhanced PA/PT contrasts for nanomedicine-related theranostics. The promising intrinsic properties of CNTs, including unique NIR optical absorption, PA/PT responses, photoluminescence, Raman scattering and other optical

effects, could be significantly enhanced by the creative merging of bio/chemical materials, including metal NPs (such as Au), organic dyes and solvents (such as ICG and ethanol), polymers (such as PEG) and biopolymers (such as polysaccharides), on their surface. Also, such mergers enable the hybrid CNTs to be more biocompatible and less toxic with better biodistribution and pharmacokinetic properties, and permit more efficient and versatile bioconjugations with targeting agents. The combination of these properties makes CNTs and their hybrids ideal multimodal platforms for PA/PT molecular imaging and PT therapy, as well as some other modalities, including Raman spectroscopy. In particular, equipped with the CNT-based contrast agents, novel *in vivo* multicolor PAFC and PT technology enables minimally invasive, highly sensitive and target specific multiplex detection and killing of solid and metastatic tumor cells and infections in static and dynamic conditions (e.g. in blood and lymph flow) that were otherwise previously difficult to achieve using conventional methods. Although this review mainly focused on CNT-based contrast agents, we have already demonstrated that the approaches and schematics presented in this review, such as *in vivo* PAFC, nanophotothermolysis of cancer and infection, plant imaging, nanothrombolysis of clots, multispectral histology, PT/PA Raman cytometry/imaging, detection of metastasis in sentinel lymph nodes, spectral hole burning and nonlinear PT/PA spectroscopy, could be used in combination with other promising contrast agents.

Acknowledgments

Vladimir P. Zharov acknowledges the National Institute of Health (NIH) grants R01 EB000873; R01 CA131164, and R21 CA139373; National Science Foundation (NSF) grant DBI-0852737; and Department of Defense (DoD) grants W88XWH-10-2-0130 and W81XWH-11-1-0123. Sanjiv Sam Gambhir acknowledges NIH grants NCI CCNE U54 CA119367 and NCI ICMIC P50 CA114747, and the Canary Foundation for Early Cancer Detection. Ekaterina I. Galanzha acknowledges DOD grant W81XWH-11-1-0129. Jin-Woo Kim acknowledges the NSF awards CMMI-0709121 and CCF-0523858, and the Arkansas Biosciences Institute. Adam de la Zerda acknowledges the Bio-X Skippy Frank Graduate Student Fellowship and the DoD Breast Cancer Research Program – Pre-doctoral Traineeship Award W81XWH-09-1-0025. Adam de la Zerda is a Damon Runyon Fellow supported by the Damon Runyon Cancer Research Foundation DRG-2094-11.

References

1. Zharov, VP.; Letokhov, VS. Laser Optoacoustic Spectroscopy. Springer; New York: 1986.
2. Wang, L., editor. Photoacoustic Imaging and Spectroscopy. Taylor & Francis/CRC Press; Boca Raton, FL: 2009.
3. Pan D, Caruthers SH, Chen J, Winter PM, SenPan A, Schmieder AH, Wickline SA, Lanza GM. Nanomedicine strategy for molecular targets with MRI and optical imaging. Future Med Chem. 2010; 2:471– 490. [PubMed: 20485473]
4. Zharov VP, Galanzha EI, Shashkov EV, Kim J-W, Khlebtsov NG, Tuchin VV. Photoacoustic flow cytometry: principle and application for real-time detection of circulating single nanoparticles, pathogens, and contrast dyes in vivo. J Biomed Opt. 2007; 12:051503. [PubMed: 17994867]
5. Galanzha EI, Shashkov EV, Tuchin VV, Zharov VP. In vivo multispectral, multiparameter, photoacoustic lymph flow cytometry with natural cell focusing, label-free detection and multicolor nanoparticle probes. Cytom A. 2008; 73:884–894.
6. de la Zerda A, et al. Carbon nanotubes as photoacoustic molecular imaging agents in living mice. Nat Nanotechnol. 2008; 3:557–562. [PubMed: 18772918]
7. de la Zerda A, et al. Ultrahigh sensitivity carbon nanotube agents for photoacoustic molecular imaging in living mice. Nano Lett. 2010; 10:2168–2172. [PubMed: 20499887]
8. Galanzha EI, Shashkov EV, Kelly T, Kim J-W, Yang L, Zharov VP. In vivo magnetic enrichment and multiplex photoacoustic detection of circulating tumour cells. Nat Nanotechnol. 2009; 4:855–860. [PubMed: 19915570]

9. Kim J-W, Galanzha EI, Shashkov EV, Moon H-M, Zharov VP. Golden carbon nanotubes as multimodal photoacoustic and photothermal high-contrast molecular agents. Nat Nanotechnol. 2009; 4:688–694. [PubMed: 19809462]
10. Galanzha EI, Shashkov EV, Kokoshka MS, Myhill JA, Zharov. In vivo noninvasive detection of metastatic cells in vasculature and sentinel lymph nodes by photoacoustic cytomery. Laser Surg Med. 2008; S20:81–82.
11. Galanzha EI, Kokoska MS, Shashkov EV, Kim J-W, Tuchin VV, Zharov VP. In vivo fiber-based multicolor photoacoustic detection and photothermal purging of metastasis in sentinel lymph nodes targeted by nanoparticles. J Biophotonics. 2009; 2:528–539. [PubMed: 19743443]
12. Wang SLN, Pramanik M, et al. In vivo carbon nanotube-enhanced non-invasive photoacoustic mapping of the sentinel lymph node. Phys Med Biol. 2009; 54:3291–3301. [PubMed: 19430111]
13. Pramanik M, Swierczewska M, Green D, Sitharaman B, Wang LV. Single-walled carbon nanotubes as a multimodal-thermoacoustic and photoacoustic-contrast agent. J Biomed Opt. 2009; 14:034018. [PubMed: 19566311]
14. Xiang L, et al. Photoacoustic molecular imaging with antibody-functionalized single-walled carbon nanotubes for early diagnosis of tumor. J Biomed Opt. 2009; 14:021008. [PubMed: 19405721]
15. Shashkov EV, Galanzha EI, Zharov VP. Photothermal and photoacoustic Raman cytometry in vitro and in vivo. Opt Express. 2010; 18:6929–6944. [PubMed: 20389713]
16. Nedosekin DA, Shashkov EV, Galanzha EI, Hennings L, Zharov VP. Photothermal multispectral image cytometry for quantitative histology of nanoparticles and micrometastasis in intact, stained and selectively burned tissues. Cytom A. 2010; 77:1049–1058.
17. Khodakovskaya MV, et al. Complex genetic, photothermal, and photoacoustic analysis of nanoparticle–plant interactions. Proc Natl Acad Sci USA. 2010 1008856108 [pii]. 10.1073/pnas.1008856108
18. Nedosekin DA, Sarimollaoglu M, Shashkov EV, Galanzha EI, Zharov VP. Ultra-fast photoacoustic flow cytometry with a 0. 5 MHz pulse repetition rate nanosecond laser. Opt Express. 2010; 18:8605–8620. [PubMed: 20588705]
19. Zharov VP, Galitovsky V, Viegas M. Photothermal detection of local thermal effects during selective nanophotothermolysis. Appl Phys Lett. 2003; 83:4897–4899.
20. Zharov VP, Galitovskaya EN, Jonson C, Kelly T. Synergistic enhancement of selective nanophotothermolysis with gold nanoclusters: potential for cancer therapy. Laser Surg Med. 2005; 37:219–226.
21. Zharov VP, Letfullin RR, Galitovskaya EN. Microbubbles-overlapping mode for laser killing of cancer cells with absorbing nanoparticle clusters. J Phys D Appl Phys. 2005; 38:2571–258.
22. Zharov VP, Kim J-W, Everts M, Curiel DT. Self-assembling nanoclusters in living system application for integrated photothermal nanodiagnostics and nanotherapy. Nanomedicine. 2005; 1:326–345. [PubMed: 17292107]
23. Zharov VP, Mercer KE, Galitovskaya EN, Smeltzer MS. Photothermal nanotherapeutics and nanodiagnostics for selective killing of bacteria targeted with gold nanoparticles. Biophys J. 2006; 90:619–628. [PubMed: 16239330]
24. Kim J-W, Galanzha EI, Shashkov EV, Kotagiri N, Zharov VP. Photothermal antimicrobial nanotherapy and nanodiagnostics with self-assembling carbon nanotube clusters. Lasers Surg Med. 2007; 39:622–634. [PubMed: 17868103]
25. Galanzha EI, Kim J-W, Zharov VP. Integrated nanotechnology-based photoacoustic and photothermal flow cytometry platform for in vivo detection and killing of circulating cancer stem cells. J Biophoton. 2009; 2:725–735.
26. Khlebtsov B, Zharov V, Melnikov A, Tuchin V, Khlebtsov N. Optical amplification of photothermal therapy with gold nanoparticles and nanoclusters. Nanotechnology. 2006; 17:5167–5179.
27. Letfullin RR, Joenathan C, George TF, Zharov VP. Laser-induced explosion of gold nanoparticles: potential for cancer therapy. Nanomedicine. 2006; 1:473–480. [PubMed: 17716149]
28. Green DE, Longtin JP, Sitharaman B. The effect of nanoparticle-enhanced photoacoustic stimulation on multipotent marrow stromal cells. ACS Nano. 2009; 3:2065–2072. [PubMed: 19606849]

29. Kang B, et al. Cancer-cell targeting and photoacoustic therapy using carbon nanotubes as ‘bomb’ agents. Small. 2009; 5:1292–1301. [PubMed: 19274646]
30. Hirsch LR, Stafford RJ, Bankson JA, et al. Nanoshell-mediated thermal therapy of tumors under magnetic resonance guidance. Proc Natl Acad Sci USA. 2003; 100:13549–13554. [PubMed: 14597719]
31. Kam NW, O’Connell M, Wisdom JA, Dai H. Carbon nanotubes as multifunctional biological transporters and near-infrared agents for selective cancer cell destruction. Proc Natl Acad Sci USA. 2005; 102:11600–11605. [PubMed: 16087878]
32. Galanzha EI, Shashkov EV, Spring P, Suen JY, Zharov VP. In vivo noninvasive label-free detection and eradication of circulating metastatic melanoma cells by two-color photoacoustic flow cytometry and a diode laser. Cancer Res. 2009; 69:7926–7934. [PubMed: 19826056]
33. Zharov VP. Ultrasharp nonlinear photothermal and photoacoustic resonances and holes beyond the spectral limit. Nat Photonics. 2011; 5:110–116.
34. Shashkov EV, Everts M, Galanzha EI, Zharov VP. Quantum dots as multimodal photoacoustic and photothermal contrast agents. Nano Lett. 2008; 8:3953–3958. [PubMed: 18834183]
35. Pustovalov VK, Smetannikov AS, Zharov VP. Photothermal and accompanied phenomena of selective nanophotothermolysis with gold nanoparticles and laser pulses. Laser Phys Lett. 2008; 5:775–792.
36. Pustovalov VK, Astafyeva LG, Galanzha EI, Zharov VP. Thermo-optical analysis and selection of the properties of absorbing nanoparticles for laser application in cancer nanotechnology. Cancer Nanotechnol. 2010; 1:35–46.
37. Nikolaev P, et al. Gas-phase catalytic growth of single-walled carbon nanotubes from carbon monoxide. Chem Phys Lett. 1999; 313:91–97.
38. Meyyappan M, et al. Carbon nanotube growth by PECVD: a review. Plasma Sources Sci Technol. 2003; 12:205.
39. Gamaly EG, Ebbesen TW. Mechanism of carbon nanotube formation in the arc discharge. Phys Rev B Condens Matter. 1995; 52:2083–2089. [PubMed: 9981282]
40. Yudasaka M, Komatsu T, Ichihashi T, Iijima S. Single-wall carbon nanotube formation by laser ablation using double-targets of carbon and metal. Chem Phys Lett. 1997; 278:102–106.
41. Kotagiri N, Kim J-W. Carbon nanotubes fed on ‘carbs’: coating of single-walled carbon nanotubes by dextran sulfate. Macromol Biosci. 2010; 10:231–238. [PubMed: 20020520]
42. Templeton AC, Hostetler MJ, Warmoth EK, Chen SW, Hartshorn CM, Krishnamurthy VM, et al. Gateway reactions to diverse, polyfunctional monolayer-protected gold clusters. J Am Chem Soc. 1998; 120:4845–4849.
43. Kim J-H, Kim J-W. Sequential solid-phase fabrication of bi-functional anchors on gold nanoparticles for controllable and scalable nanoscale structure assembly. Langmuir. 2008; 24:5667–5671. [PubMed: 18465887]
44. Kim J-H, Kim J-W. Simultaneously controlled directionality and valency on a water-soluble gold nanoparticle precursor for aqueous-phase anisotropic self-assembly. Langmuir. 2010; 26:18634–18638. [PubMed: 21117631]
45. Bell AG. On the production and reproduction of sound by light. Am J Sci. 1880; 20:305–324.
46. O’Connell MJ, et al. Band gap fluorescence from individual single-walled carbon nanotubes. Science. 2002; 297:593–596. [PubMed: 12142535]
47. Rao AM, et al. Diameter-selective Raman scattering from vibrational modes in carbon nanotubes. Science. 1997; 275:187–191. [PubMed: 8985007]
48. Keren S, et al. Noninvasive molecular imaging of small living subjects using Raman spectroscopy. Proc Natl Acad Sci USA. 2008; 105:5844–5849. [PubMed: 18378895]
49. Liu Z, et al. Circulation and long-term fate of functionalized, biocompatible single-walled carbon nanotubes in mice probed by Raman spectroscopy. Proc Natl Acad Sci USA. 2008; 105:1410–1415. [PubMed: 18230737]
50. Zavaleta C, et al. Noninvasive Raman spectroscopy in living mice for evaluation of tumor targeting with carbon nanotubes. Nano Lett. 2008; 8:2800–2805. [PubMed: 18683988]

51. Biris AS, Galanzha EI, Li Z, Mahmood M, Xu Y, Zharov VP. In vivo Raman flow cytometry for real-time detection of carbon nanotube kinetics in lymph, blood, and tissues. J Biomed Opt. 2009; 14:021006. [PubMed: 19405719]
52. Hurt RH, Monthioux M, Kane A. Toxicology of carbon nanomaterials: status, trends, and perspectives on the special issue. Carbon. 2006; 44:1028–1033.
53. Smart SK, Cassady AI, Lu GQ, Martin DJ. The biocompatibility of carbon nanotubes. Carbon. 2006; 44:1034–1047.
54. Poland CA, et al. Carbon nanotubes introduced into the abdominal cavity of mice show asbestos-like pathogenicity in a pilot study. Nat Nanotechnol. 2008; 3:423–428. [PubMed: 18654567]
55. Schipper ML, et al. A pilot toxicology study of single-walled carbon nanotubes in a small sample of mice. Nat Nanotechnol. 2008; 3:216–221. [PubMed: 18654506]
56. Eghtedari M, et al. High sensitivity of in vivo detection of gold nanorods using a laser optoacoustic imaging system. Nano Lett. 2007; 7:1914–1918. [PubMed: 17570730]
57. Kim J-W, Moon H-M, Benamara M, Sakon J, Salamo G, Zharov VP. Aqueous-phase synthesis of monodisperse plasmonic gold nanocrystals using shortened single-walled carbon nanotubes. Chem Commun. 2010; 46:7142–7144.
58. Landsman ML, Kwant G, Mook GA, Zijlstra WG. Light-absorbing properties, stability, and spectral stabilization of indocyanine green. J Appl Physiol. 1976; 40:575–583. [PubMed: 776922]
59. Liu Z, et al. In vivo biodistribution and highly efficient tumour targeting of carbon nanotubes in mice. Nat Nanotechnol. 2007; 2:47–52. [PubMed: 18654207]
60. Link S, Mohamed MB, El-Sayed MA. Simulation of the optical absorption spectra of gold nanorods as a function of their aspect ratio and the effect of the medium dielectric constant. J Phys Chem B. 1999; 103:3073–3077.
61. Wu AM, Senter PD. Arming antibodies: prospects and challenges for immunoconjugates. Nat Biotechnol. 2005; 23:1137–1146. [PubMed: 16151407]
62. Niyogi S, et al. Chemistry of single-walled carbon nanotubes. Acc Chem Res. 2002; 35:1105–1113. [PubMed: 12484799]
63. Rosca ID, Watari F, Uo M, Akasaka T. Oxidation of multiwalled carbon nanotubes by nitric acid. Carbon. 2005; 43:3124–3131.
64. Zeng L, Alemany L, Edwards C, Barron A. Demonstration of covalent sidewall functionalization of single wall carbon nanotubes by NMR spectroscopy: side chain length dependence on the observation of the sidewall carbons. Nano Res. 2008; 1:72–88.
65. Liu Z, Sun X, Nakayama-Ratchford N, Dai H. Chemistry on water-soluble carbon nanotubes for drug loading and delivery. ACS Nano. 2007; 1:50–56. [PubMed: 19203129]
66. Zhao B, Hu H, Yu A, Perea D, Haddon RC. Synthesis and characterization of water soluble single-walled carbon nanotube graft copolymers. J Am Chem Soc. 2005; 127:8197–8203. [PubMed: 15926849]
67. Lee KM, Li L, Dai L. Asymmetric end-functionalization of multi-walled carbon nanotubes. J Am Chem Soc. 2005; 127:4122–4123. [PubMed: 15783165]
68. Coleman KS, Bailey SR, Fogden S, Green ML. Functionalization of single-walled carbon nanotubes via the Bingel reaction. J Am Chem Soc. 2003; 125:8722–8723. [PubMed: 12862456]
69. Georgakilas V, et al. Organic functionalization of carbon nanotubes. J Am Chem Soc. 2002; 124:760–761. [PubMed: 11817945]
70. Tagmatarchis N, Prato M. Functionalization of carbon nanotubes via 1,3-dipolar cycloadditions. J Mater Chem. 2004; 14:437–439.
71. Guldi DM, Taieb H, Rahman GMA, Tagmatarchis N, Prato M. Novel Photoactive single-walled carbon nanotube-porphyrin polymer wraps: efficient and long-lived intracomplex charge separation. Adv Mater. 2005; 17:871–875.
72. Chen RJ, Zhang Y, Wang D, Dai H. Noncovalent sidewall functionalization of single-walled carbon nanotubes for protein immobilization. J Am Chem Soc. 2001; 123:3838–3839. [PubMed: 11457124]
73. Wu P, et al. Biocompatible carbon nanotubes generated by functionalization with glycodendrimers. Angew Chem Int Edn. 2008; 47:5022–5025.

74. Kim J-W, Kotagiri N, Kim J-H, Deaton R. In situ fluorescence microscopy visualization and characterization of nanometer-scale carbon nanotubes labeled with 1-pyrenebutanoic acid, succinimidyl ester. Appl Phys Lett. 2006; 88:213110.

75. Zheng M, et al. DNA-assisted dispersion and separation of carbon nanotubes. Nat Mater. 2003; 2:338–342. [PubMed: 12692536]

76. Moon H, Chang C, Lee D-K, Choi H. Effect of nucleases on the cellular internalization of fluorescent labeled DNA-functionalized single-walled carbon nanotubes. Nano Res. 2008; 1:351–360.

77. Star A, Steuerman DW, Health JR, Stoddart JF. Starched carbon nanotubes. Angew Chem Int Edn. 2002; 41:2508–2512.

78. Kotagiri N, Kim J-W. Carbon nanotubes fed on 'carbs': coating of single-walled carbon nanotubes by dextran sulfate. Macromol Biosci. 2010; 10:231–238. [PubMed: 20020520]

79. Liu Z, Tabakman S, Welsher K, Dai H. Carbon nanotubes in biology and medicine: in vitro and in vivo detection, imaging and drug delivery. Nano Res. 2009; 2:85–120. [PubMed: 20174481]

80. Templeton AC, Hostetler MJ, Warmoth EK, Chen SW, Hartshorn CM, Krishnamurthy VM, et al. Gateway reactions to diverse, polyfunctional monolayer-protected gold clusters. J Am Chem Soc. 1998; 120:4845–4849.

81. Dumortier H, et al. Functionalized carbon nanotubes are non-cytotoxic and preserve the functionality of primary immune cells. Nano Lett. 2006; 6:1522–1528. [PubMed: 16834443]

82. Schipper ML, et al. A pilot toxicology study of single-walled carbon nanotubes in a small sample of mice. Nat Nanotechnol. 2008; 3:216–221. [PubMed: 18654506]

83. Mahmood M, Mocan T, Iancu C, Mocan L, Iancu DT, Xu Y, Dervishi E, Li Z, Biris AR, Agarwal R, Ali N, Galanzha EI, Biris AS, Zharov VP. Synergistic enhancement of cancer therapy using a combination of carbon nanotubes and antitumor drug. J Nanomed. 2009; 4:72205.

84. Ding L, et al. Molecular characterization of the cytotoxic mechanism of multiwall carbon nanotubes and nano-onions on human skin fibroblast. Nano Lett. 2005; 5:2448–2464. [PubMed: 16351195]

85. Cui D, Tian F, Ozkan CS, Wang M, Gao H. Effect of single wall carbon nanotubes on human HEK293 cells. Toxicol Lett. 2005; 155:73–85. [PubMed: 15585362]

86. Lam CW, James JT, McCluskey R, Hunter RL. Pulmonary toxicity of single-wall carbon nanotubes in mice 7 and 90 days after intratracheal instillation. Toxicol Sci. 2004; 77:126–134. [PubMed: 14514958]

87. Shvedova AA, et al. Unusual inflammatory and fibrogenic pulmonary responses to single-walled carbon nanotubes in mice. Am J Physiol Lung Cell Mol Physiol. 2005; 289:L698–708. [PubMed: 15951334]

88. Warheit DB, et al. Comparative pulmonary toxicity assessment of single-wall carbon nanotubes in rats. Toxicol Sci. 2004; 77:117–125. [PubMed: 14514968]

89. Muller J, et al. Respiratory toxicity of multi-wall carbon nanotubes. Toxicol Appl Pharmacol. 2005; 207:221–231. [PubMed: 16129115]

90. Poland CA, et al. Carbon nanotubes introduced into the abdominal cavity of mice show asbestos-like pathogenicity in a pilot study. Nat Nanotechnol. 2008; 3:423–428. [PubMed: 18654567]

91. Bottini M, et al. Multi-walled carbon nanotubes induce T lymphocyte apoptosis. Toxicol Lett. 2006; 160:121–126. [PubMed: 16125885]

92. Sayes CM, et al. Functionalization density dependence of single-walled carbon nanotubes cytotoxicity in vitro. Toxicol Lett. 2006; 161:135–142. [PubMed: 16229976]

93. Liu Z, Winters M, Holodniy M, Dai H. siRNA delivery into human T cells and primary cells with carbon-nanotube transporters. Angew Chem Int Edn. 2007; 46:2023–2027.

94. Chen X, Lee GS, Zettl A, Bertozzi CR. Biomimetic engineering of carbon nanotubes by using cell surface mucin mimics. Angew Chem Int Edn. 2004; 43:6111–6116.

95. Chen X, et al. Interfacing carbon nanotubes with living cells. J Am Chem Soc. 2006; 128:6292–6293. [PubMed: 16683774]

96. Wu W, et al. Targeted delivery of amphotericin B to cells by using functionalized carbon nanotubes. Angew Chem Int Edn. 2005; 44:6358–6362.

97. Chin SF, et al. Amphiphilic helical peptide enhances the uptake of single-walled carbon nanotubes by living cells. Exp Biol Med Maywood. 2007; 232:1236–1244. [PubMed: 17895532]

98. Yehia HN, et al. Single-walled carbon nanotube interactions with HeLa cells. J Nanobiotechnol. 2007; 5:8.

99. Yang ST, et al. Long-term accumulation and low toxicity of single-walled carbon nanotubes in intravenously exposed mice. Toxicol Lett. 2008; 181:182–189. [PubMed: 18760340]

100. Liu Z, Sun X, Nakayama-Ratchford N, Dai H. Supramolecular chemistry on water-soluble carbon nanotubes for drug loading and delivery. ACS Nano. 2007; 1:50–56. [PubMed: 19203129]

101. Murphy CJ, et al. Gold nanoparticles in biology: beyond toxicity to cellular imaging. Acc Chem Res. 2008; 41:1721–1730. [PubMed: 18712884]

102. Lewinski N, Colvin V, Drezek R. Cytotoxicity of nanoparticles. Small. 2008; 4:26–49. [PubMed: 18165959]

103. Jan E, et al. High-content screening as a universal tool for fingerprinting of cytotoxicity of nanoparticles. ACS Nano. 2008; 2:928–938. [PubMed: 19206490]

104. Pernodet N, et al. Effects of citrate/gold nanoparticles on human dermal fibroblasts. Small. 2006; 2:766–773. [PubMed: 17193121]

105. Shukla R, et al. Biocompatibility of gold nanoparticles and their endocytotic fate inside the cellular compartment: a microscopic overview. Langmuir. 2005; 21:10644–10654. [PubMed: 16262332]

106. Connor EE, Mwamuka J, Gole A, Murphy CJ, Wyatt MD. Gold nanoparticles are taken up by human cells but do not cause acute cytotoxicity. Small. 2005; 1:325–327. [PubMed: 17193451]

107. Singh R, Pantarotto D, Lacerda L, Pastorin G, Klumpp C, Prato M, Bianco A, Kostarelos K. Tissue biodistribution and blood clearance rates of intravenously administered carbon nanotube radiotracers. Proc Natl Acad Sci USA. 2006; 103:3357–3362. [PubMed: 16492781]

108. Lacerda L, et al. Dynamic imaging of functionalized multi-walled carbon nanotube systemic circulation and urinary excretion. Adv Mater. 2008; 20:225–230.

109. Deng X, Jia G, Wang H, Sun H, Wang X, Yang S, Wang T, Liu Y. Translocation and fate of multi-walled carbon nanotubes in vivo. Carbon. 2007; 45:1419–1424.

110. Deng XY, Yang ST, Nie HY, Wang HF, Liu YF. A generally adoptable radiotracing method for tracking carbon nanotubes in animals. Nanotechnology. 2008; 19:075101. [PubMed: 21817626]

111. Yang ST, et al. Covalently PEGylated carbon nanotubes with stealth character in vivo. Small. 2008; 4:940–944. [PubMed: 18574799]

112. Zharov VP, Galanzha EI, Shashkov EV, Khlebtsov NG, Tuchin VV. In vivo photoacoustic flow cytometry for monitoring of circulating single cancer cells and contrast agents. Opt Lett. 2006; 31:3623–3625. [PubMed: 17130924]

113. Tsivgoulis G, Culp WC, Alexandrov AV. Ultrasound enhanced thrombolysis in acute arterial ischemia. Ultrasonics. 2008; 48:303–311. [PubMed: 18511094]

114. Kim C, Oin R, Xu JS, Wong LV, Xu R. Multifunctional microbubbles and nanobubbles for photoacoustic and ultrasound imaging. J Biomed Opt. 2010; 15:010510. [PubMed: 20210423]

115. Yakovlev VV, Zhang HF, Noojin GD, Denton ML, Thomas RJ, Scully MO. Stimulated Raman photoacoustic imaging. Proc Natl Acad Sci USA. 2010; 107:20335–20339. [PubMed: 21059930]

116. Biris AS, Boldor D, Parker J, Li Z, Galanzha E, Zharov VP. Nanophotothermolysis of scattered cancer cells with carbon nanotubes guided by time-resolved thermal imaging. J Biomed Opt. 2009; 14:021007-1-6. [PubMed: 19405720]

117. Galanzha EI, Tuchin VV, Zharov VP. Advances in small animal mesentery models for in vivo flow cytometry, dynamic microscopy, and drug screening (review). Wld J Gastroenterol. 2007; 13:192–218.

118. Akchurin G, et al. Gold nanoshell photomodification under single nanosecond laser pulse accompanied by color-shifting and bubble formation phenomena. Nanotechnology. 2008; 19:015701. [PubMed: 21730542]

119. Zharov VP, Galanzha EI, Menyaev YA, Tuchin VV. In vivo high-speed imaging of individual cells in fast blood flow. J Biomed Opt. 2006; 11:054034. [PubMed: 17092183]

120. Moerner, WE.; Bjorklund, GC. Persistent Spectral Hole-burning: Science and Applications. Springer; New York: 1988.
121. Moon H-M, Kim J-W. Carbon nanotube clusters as universal bacterial adsorbents and magnetic separation agents. Biotechnol Prog. 2010; 26:179–185. [PubMed: 19856390]
122. Zharov VP, Galanzha EI, Tuchin VV. Photothermal imaging of moving cells in lymph and blood flow in vivo. Proc SPIE. 2004; 5320:185–195.
123. Kudryashov SI, Allen SD, Galanzha EI, Galitovskaya E, Zharov VP. Photoacoustics of individual live cells and particles. Proc SPIE. 2006; 6086:60860J.
124. Zharov VP. Revolutionizing blood testing. Eur J Int Innov. 2010 Jun.:97–99. Healthcare.
125. Olszewski WL, Tárnok A. Photoacoustic listening of cells in lymphatics: research art or novel clinical noninvasive lymph test. Cytom A. 2008; 73A:1111–1113.

Biographies

Adam de la Zerda is a Ph.D. candidate of Electrical Engineering at Stanford University. His work on Photoacoustic Molecular Imaging has awarded him with over 10 awards including the Best Poster Presentation at SPIE Photonics West 2009, the Young Investigator Award at the World Molecular Imaging Congress 2008, and the DoD Breast Cancer Research Award. He holds a number of patents and over 15 publications in leading journals including *Nature Nanotechnology* and *PNAS*. He holds a B.Sc. in Computer Engineering from the Technion – Israel Institute of Technology, where he graduated *Summa Cum Laude*.

Jin-Woo Kim is a Professor of Biological and Biomedical Engineering at University of Arkansas, Fayetteville, AR, USA. His expertise spans interdisciplinary fields of engineering, biology, chemistry and nanotechnology with primary research interest in the area of Bio/Nano Technology. Particular emphases have been given to aqueous-phase self-organizations of nanomaterials and their biological and biomedical applications, in particular bio-driven nanostructure self-assembly, nanoscale bio/abio interfacing and nanoparticle-based theranostics. He has over 80 peer-reviewed publications in the field.

Ekaterina Galanzha is an Assistant Professor, and the leading scientist of the Phillips Classic Laser and Nanomedicine Laboratories at the University of Arkansas for Medical Sciences. She received MD, PhD and DSc degrees from Saratov Universities in Russia. She has over 50 publications, and 3 books in the field of cell biology, experimental medicine, biophotonic, and nanomedicine with a focus on interdisciplinary lymphatic and cancer research. She is a co-inventor of the in vivo multicolor photoacoustic blood and lymph flow cytometry.

Vladimir Zharov is a Professor of Biomedical Engineering, Director of Laser Research, and head of the Phillips Classic Laser and Nanomedicine Laboratories at University of Arkansas for Medical Sciences. He received PhD and DSc degrees from Bauman Moscow State Technical University and completed a postdoctoral fellowship at Lawrence Berkeley National Laboratory. He has over 200 publications, 5 books, and 45 patents in the field of laser spectroscopy, biophotonics, nanomedicine, and in vivo flow cytometry. He is the State Prize Winner in Russia, and the first recipient of the US Maiman Award.

Dr. Sanjiv Sam Gambhir is the Virginia & D.K. Ludwig Professor of Radiology and Bioengineering, Director of the Molecular Imaging Program, and head of Nuclear Medicine at Stanford University. He also heads up the new Canary Center at Stanford for Cancer Early Detection. He directs over 200 scientists at Stanford as well as 30 members of his own research laboratory and focuses on the multimodality molecular imaging of cancer. He has over 375 publications in the field and over 30 patents pending or granted. He was elected to the Institute of Medicine of the US National Academies in 2008.

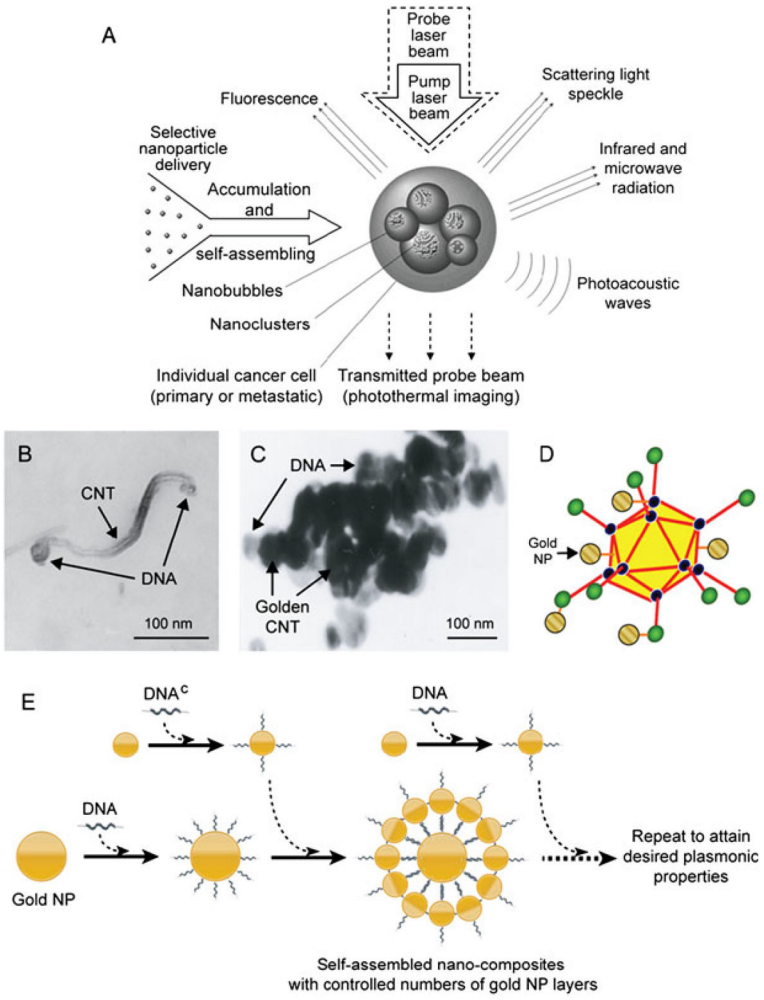

Figure 1.

(A) Principle of nanodiagnostics and nanotherapeutics with self-assembled nanoclusters. (B–E) Examples of hybrid and clustered nanoparticles (NPs): (B) site-specific functionalization of DNA to tips of carbon nanotube (CNT); (C) DNA-guided clustering of gold-coated CNTs; (D) adenoviral vector with gold NPs clustered in capsid; and (E) Schematic of DNA-directed self-assembly of nanocomposites with multi-layers of gold NPs with multiplex, multicolor and multifunctional capabilities based on the target theranostics tasks. Reproduced with permission from Zharov *et al.* (22).

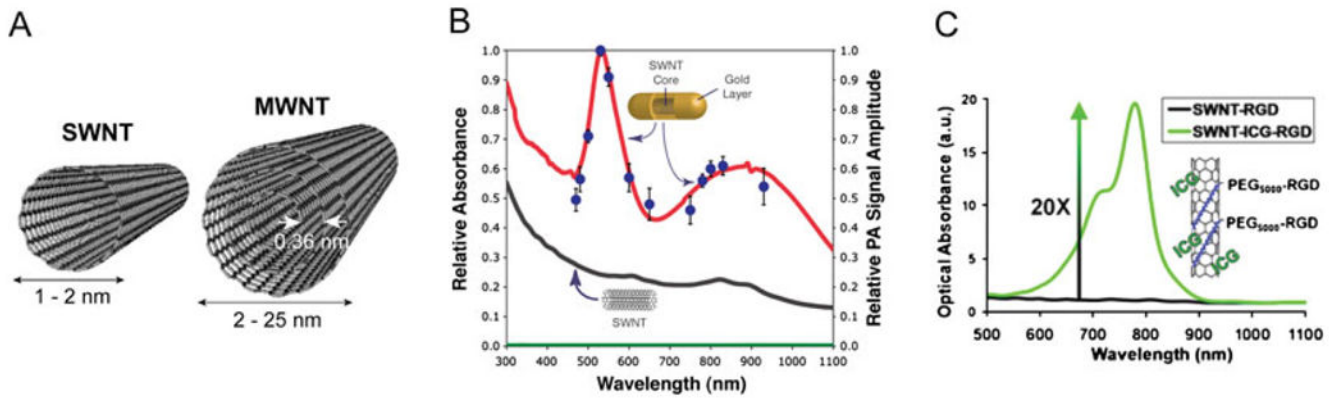

Figure 2.

(A) Schematic of single-walled and multi-walled carbon nanotubes (SWNT and MWNT, respectively). (B) Absorption spectra of SWNTs and golden carbon nanotubes (GNTs), and photoacoustic (PA) spectra of GNTs. Lines represent normalized optical spectra (left vertical axis) of GNTs in water (red curve), SWNTs in water (black curve) and water only (green curve) and the dots represent normalized PA signal amplitude (blue dots, right axis) of GNTs in water. The concentration of the SWNTs is ~35 times higher than that of GNTs; hence, 85- to 100-fold enhanced NIR contrast is achieved by the hybrid GNTs. Reproduced with permission from Kim *et al.* (9). (C) Optical absorption spectrum of SWNT-RGD (black curve) and indocyanine green-enhanced SWNT-RGD (SWNT-ICG-RGD, green curve). The optical absorbance spectrum of plain SWNT-RGD is relatively flat with slight gradual absorption decrease as the wavelength increase. However, by attaching a large number of ICG molecules to the SWNT surface, a 20-fold increase in optical absorption results at 780 nm. Reproduced with permission from de la Zerda *et al.* (7).

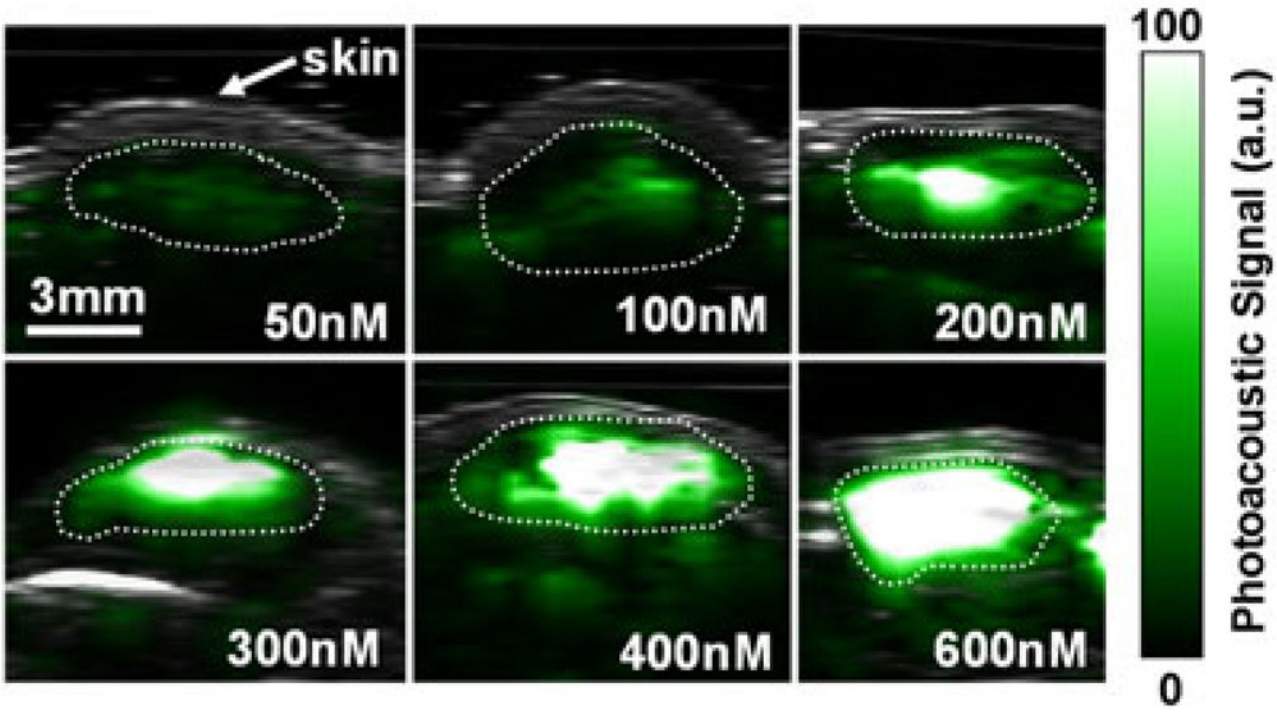

Figure 3.

Photoacoustic (PA) detection of single-walled carbon nano-tube (SWNTs) in living mice. Mice were injected subcutaneously with SWNTs at increasing concentrations from 50 to 600 nM. An ultrasound image slice (gray) showing the skin level was overlaid on the PA image (green) which visualized the SWNT PA contrast. The dotted lines on the images illustrate the edges of each inclusion. The PA signal produced by 50 nM of SWNT is equal to the average PA background signal produced by tissues. Reproduced with permission from de la Zerda *et al.* (6).

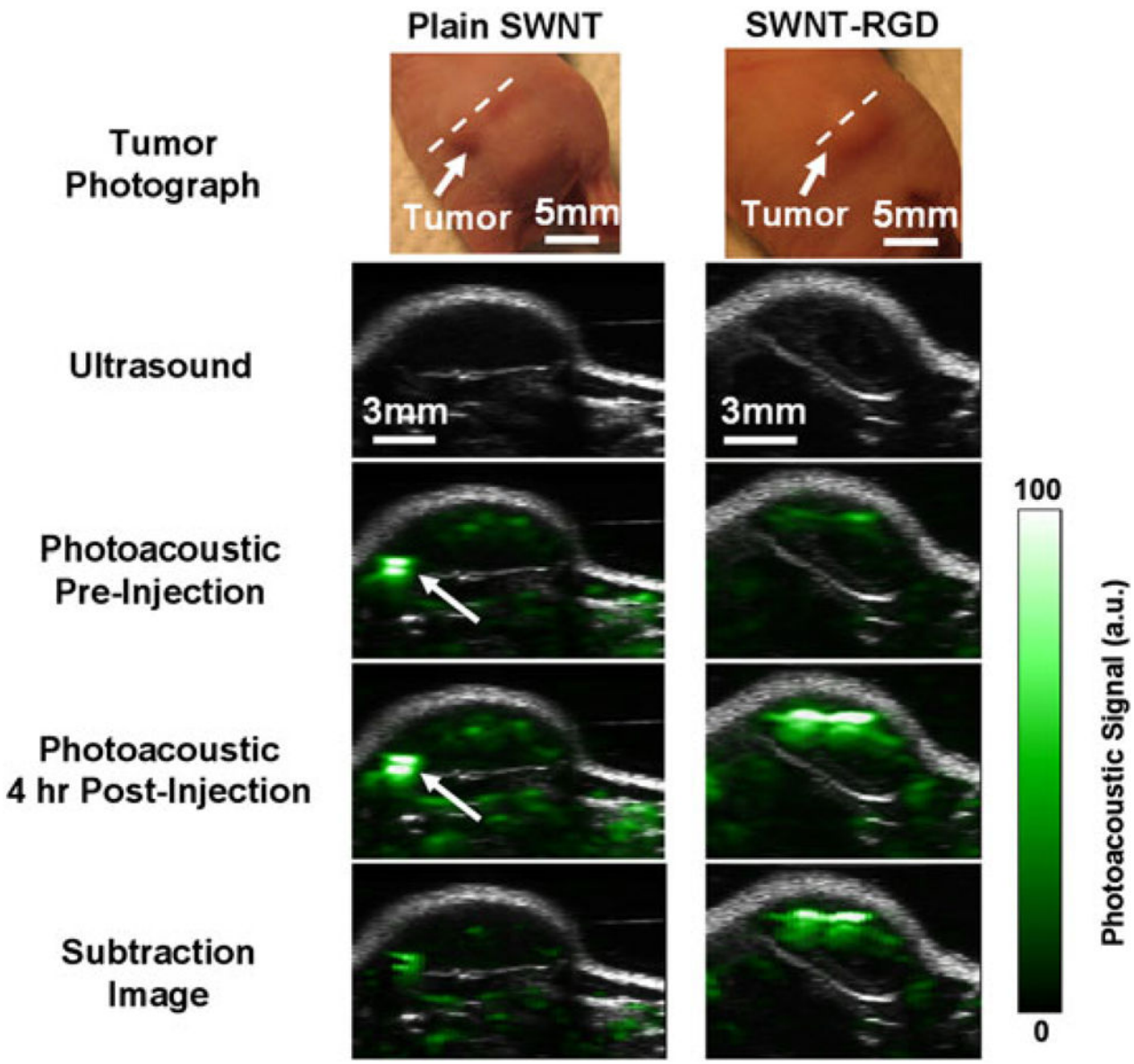

Figure 4.

Single-walled carbon nanotube arginine–glycine–aspartic acid (SWNT-RGD) tumor targeting in living mice. Ultrasound (gray) and photoacoustic (PA) (green) images of a vertical slice (white dotted line) through the tumors of mice injected with SWNT-RGD (right column) and control plain SWNTs (left column). Subtraction images were calculated as 4 h post-injection minus pre-injection to remove tissue background signal from the PA image. Mice injected with SWNT-RGD showed an averaged 7-fold PA signal increase in the tumor over mice injected with control untargeted SWNTs. The high PA signal in the mouse injected with plain SWNTs (indicated by the white arrow) is not seen in the subtraction image, suggesting that it is due to a large blood vessel and not SWNTs. Reproduced with permission from de la Zerda *et al.* (6).

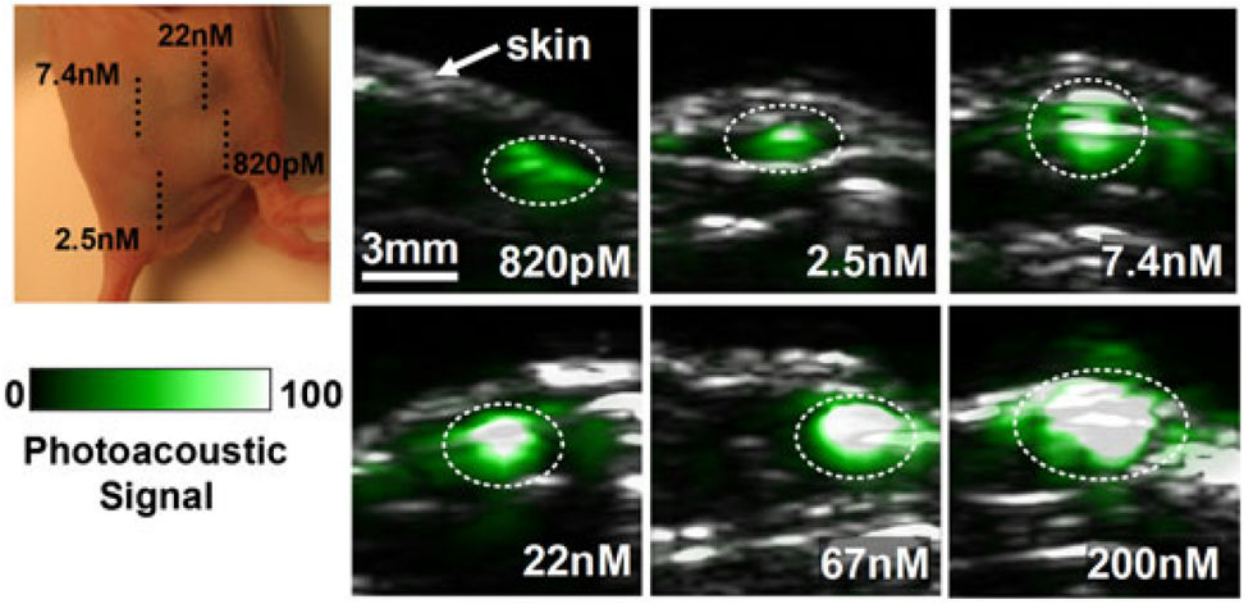

Figure 5.

Photoacoustic (PA) detection of single-walled carbon nanotube indocyanine green (SWNT-ICG) in living mice. Vertical slices of ultrasound images (gray) and PA images (green) of mice injected subcutaneously with SWNT-ICG-RGD at concentrations of 0.82–200 nM (dotted black line). The white dotted lines on the images illustrate the approximate edges of each inclusion. Quantitative analysis of the images estimated that 170 pM of SWNT-ICG-RGD gives the equivalent PA signal as the tissue background. Reproduced with permission from de la Zerda *et al.* (7).

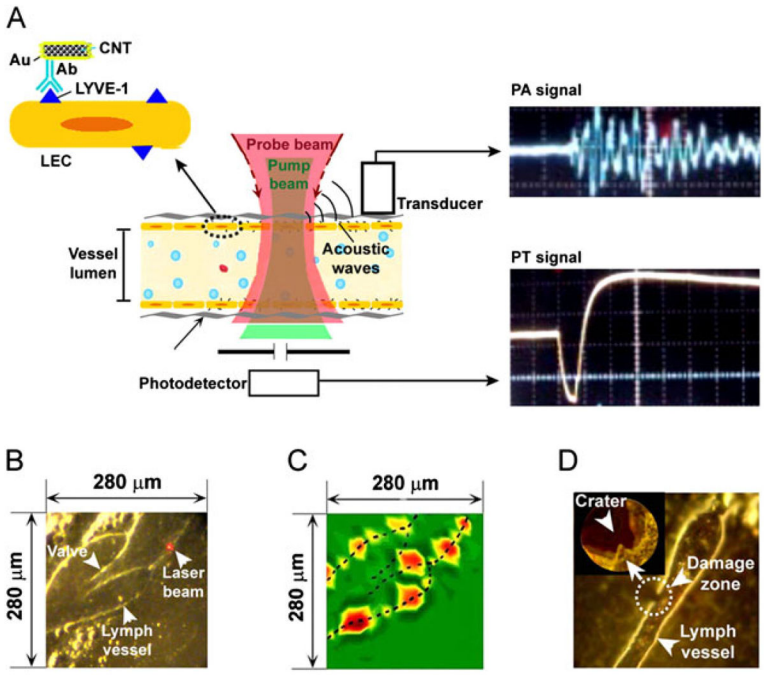

Figure 6.

In vivo photoacoustic/photothermal (PA/PT) molecular mapping of lymphatic vessels in mouse mesentery targeted by conjugated gold nanotubes (GNTs). (A) Schematic. (B) Fragment of mouse mesentery. (C) PA map of LYVE-1 receptor distribution. (D) Laser-induced localized (~10 μm in diameter) lymphatic wall damage around GNTs targeted to LYVE-1. Laser parameters: wavelength, 850 nm; pulse width, 8 ns; fluences, 35 mJ/cm^2 (C) and 80 mJ/cm^2 (D). Reproduced with permission from Kim *et al.* (9).

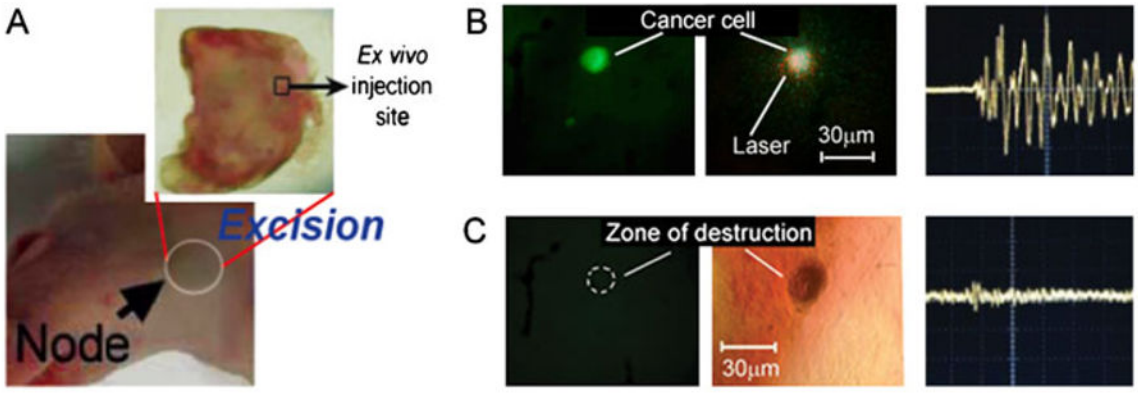

Figure 7.

Photothermal nanotherapy of breast cancer cells (MDA-MB-231) double-labeled by gold nanotube-folates and FITC after their injection in the lymph node *ex vivo*. (A) Excision of lymph node from an intact mouse. The hollow black square indicates the *ex vivo* injection site of the tumor cells. (B) Fluorescent image (left) and photoacoustic (PA) signal (right) of targeted cancer cells within the lymph node at laser fluence of 20 mJ/cm^2 at 850 nm. (C) Fluorescent image (left) and PA signal (right) as well as transmission microscopy image (middle) of the targeted cancer cells (same as B) within the lymph node after applying one laser pulse at 100 mJ/cm^2 with laser beam diameter of 100 μm. The dashed circle in (C) indicates the location of a fluorescent signal before the one-purse application of the relatively high laser. Reproduced with permission from Kim *et al.* (9).

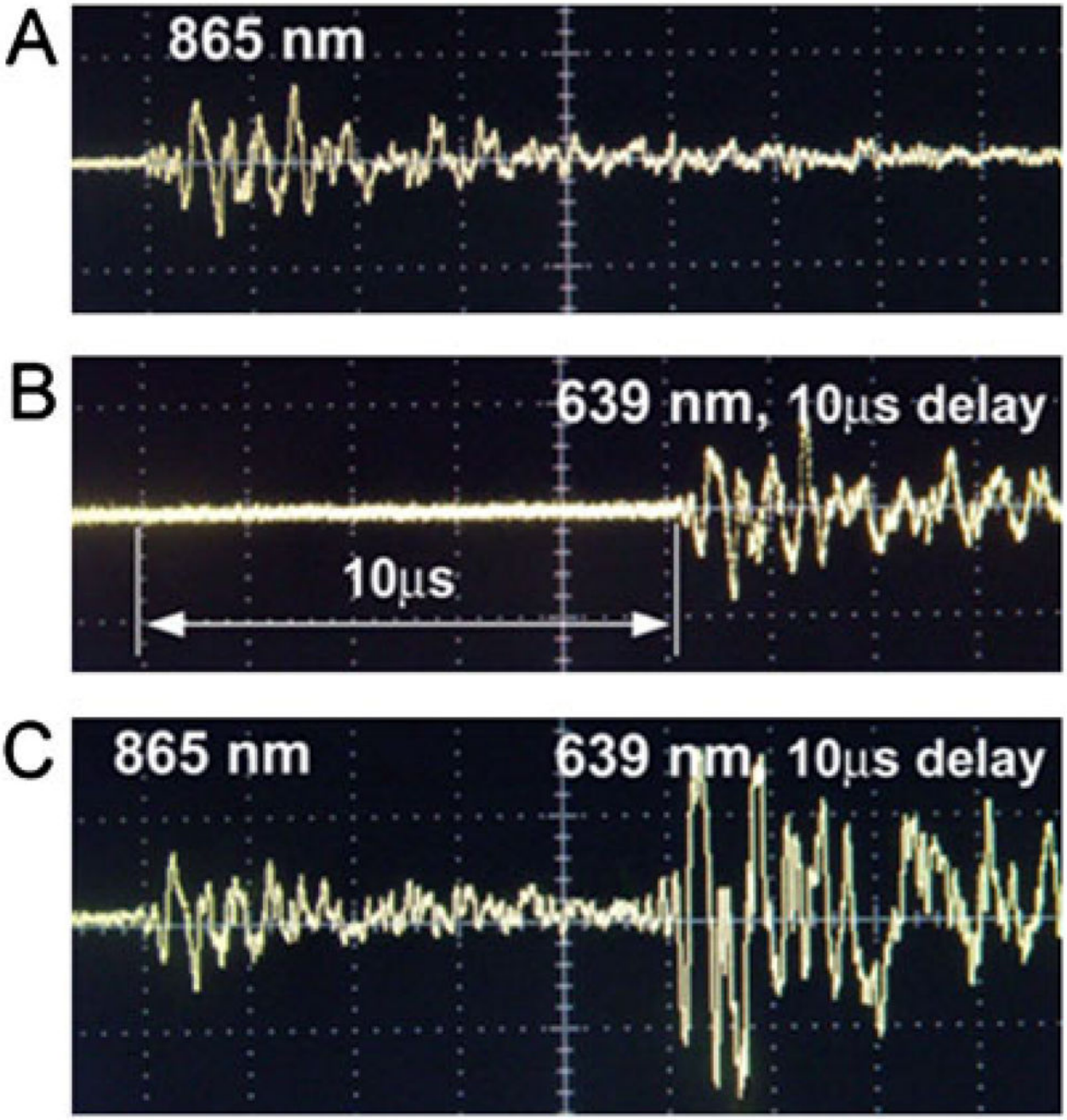

Figure 8.

Photoacoustic (PA) signals in the mesenteric lymph vessels of rats. (A) Apoptotic lymphocytes labeled with GNSs (865 nm, 35 mJ/cm^2). (B) Necrotic lymphocytes labeled with GNRs (639 nm, 25 mJ/cm^2). (C) Live neutrophils labeled with carbon nanotubes absorbing at both wavelengths. Reproduced with permission from Galanzha *et al.* (5).

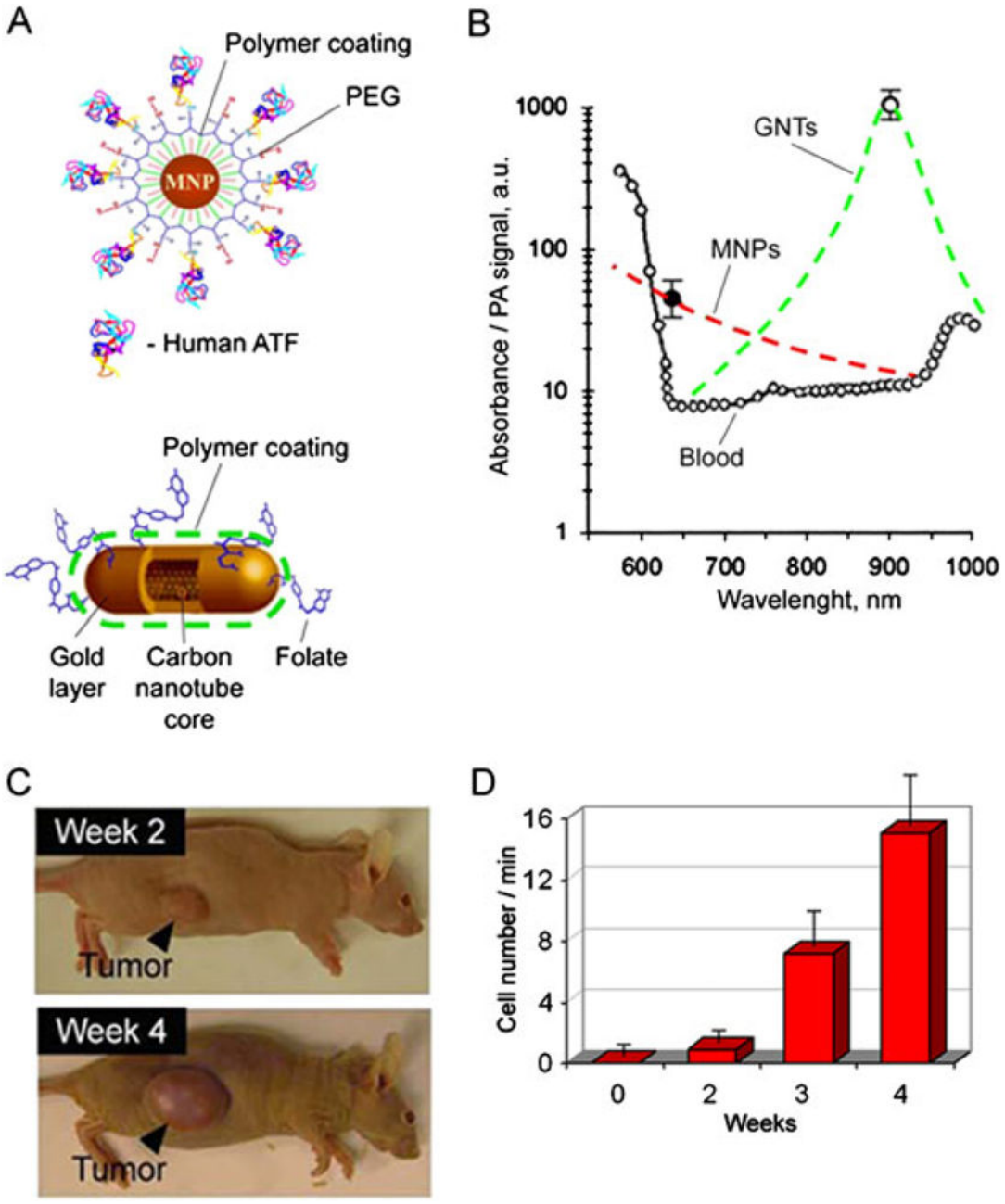

Figure 9.

In vivo multiplex two-color photoacoustic (PA) detection of circulating tumor cells (CTCs). (A) The 10 nm magnetic NPs (MNPs) coated with amphiphilic triblock polymers, polyethylene glycol (PEG) and the amino-terminal fragment of urokinase plasminogen activator (ATF). The 12 × 98 nm GNTs coated with PEG and folic acid. (B) PA spectra of ~70 μm veins in mouse ear (open circles). Absorption spectra of the MNPs and GNTs (dashed curves) normalized to PA signals from CTC labeled with MNPs (black circle) and GNTs (open circle). (C) The size of the primary breast cancer xenografts at different time

stages of tumor development. (D) Average rate of CTCs in mouse ear vein. Reproduced with permission from Galanzha *et al.* (8).

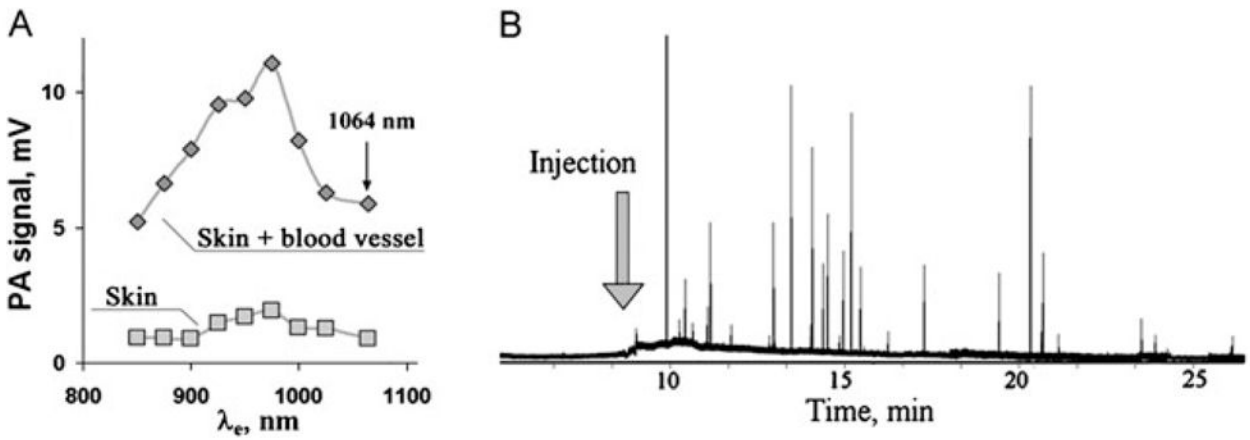

Figure 10.

(A) Photoacoustic (PA) spectra of mouse skin alone and skin with blood vessels obtained with tunable optical parametric oscillator system. (B) Traces of PA signals from circulating carbon nanotubes (CNTs) in mouse ear blood microvessels after injection of 50 μL CNTs solution in phosphate- buffered saline (2.2 mg/ml). Laser parameters: wavelength 1064 nm, pulse rate 100 kHz, laser beam shape, 20 × 100 μm. Reproduced with permission from Nedosekin *et al.* (18).

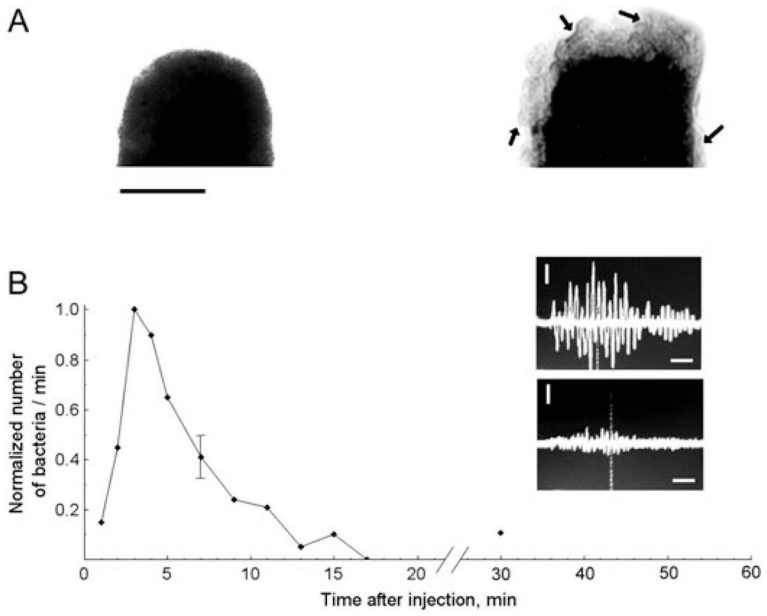

Figure 11.

(A) TEM images of an *E. coli* fragment before (left) and after (right) incubation with carbon nanotubes (CNTs). Arrows indicate CNT clusters within the bacteria wall structure. Scale bars represent 500 nm. (B) Normalized number of circulating *E. coli* in blood microvessels of mouse ear as a function of time post injection. Oscilloscope signals: photoacoustic signals from labeled *E. coli* in blood (top) and from blood alone (bottom). Amplitude/time scale: 200 mV/div/2 μs/div. Scale bar represents amplitude/time scale: 200 mV/div/2 μs/div, respectively. Laser parameters: wavelength 850 nm, laser fluence 50 mJ/cm^2. Reproduced with permission from Zharov *et al.* (4).

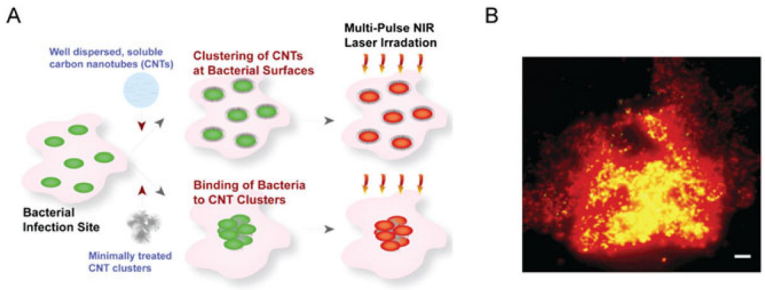

Figure 12.

Photothermal antimicrobial nanotherapy with carbon nanotube (CNT) clusters. (A) Schematic of CNT delivery to the infected site, their self- assembly at the bacterial surfaces or spontaneous bacterial adsorption to the large CNT clusters, and their NIR responsiveness to kill the bacteria. Cartoon shows live (green) and dead (red) bacteria. (B) Epi-fluorescence images of damaged *E. coli* adsorbed on clustered CNT after single-pulse laser exposure (1064 nm, 0.5 J/cm^2, 12 ns). Scale bar is 5 μm. Reproduced with permission from Kim *et al.* (24).

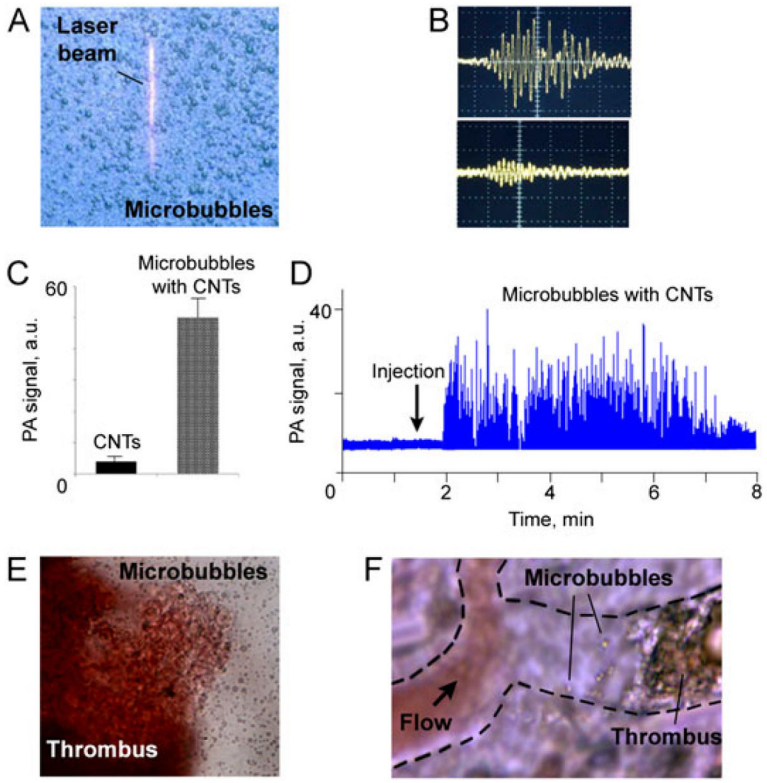

Figure 13.

(A) Optical image of 0.5–2 μm microbubbles with linear laser beam. (B) Typical linear photoacoustic signals from microbubbles with carbon nanotube (CNTs) (top) and surrounding contaminated medium (bottom). Amplitude/time scale: (top) 50 mV/div and 2 μs/div, (bottom) 10 mV/div and 2 μs/div. Laser parameters: wavelength 850 nm, energy fluence 20 mJ/cm^2. (C) Nonlinear signals from CNTs in water suspension (left) and from microbubbles with CNTs (right) at similar concentration of CNTs. Laser parameters: wavelength 850 nm, energy fluence 100 mJ/cm^2. (D) Clearance of circulating microbubbles with CNTs in mouse ear microvessels. (E) Optical image of thrombus with microbubbles *in vitro*. (F) *In vivo* animal model (rat mesentery) for study selective nanophotothrombolysis with nanoparticles and microbubbles.

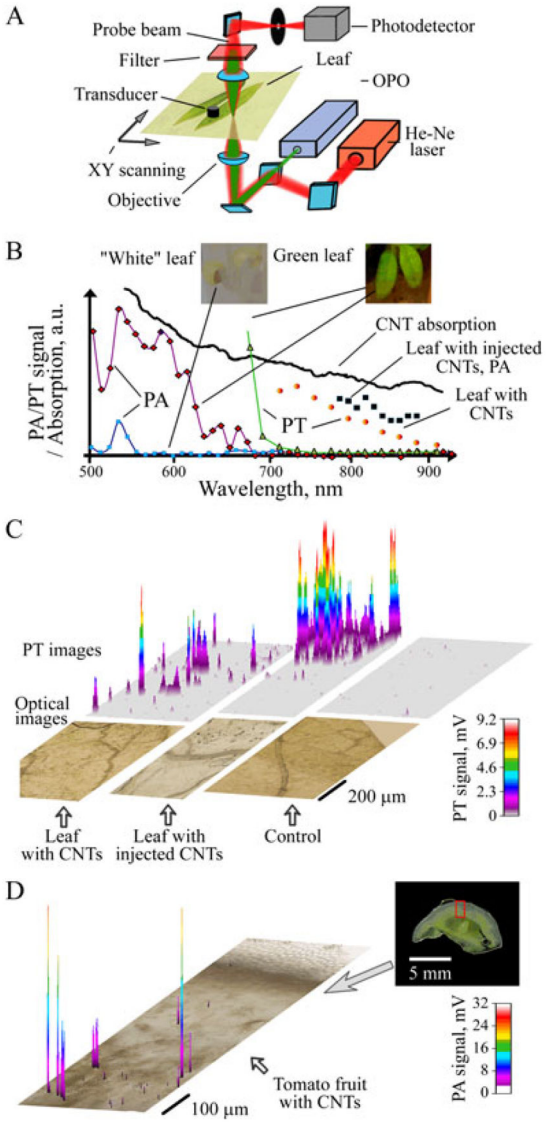

Figure 14.

Photothermal (PT) and photoacoustic (PA) detection of multi- walled carbon nanotube (CNTs) in tomato leaves. (A) Schematic of integrated PA/PT scanning cytometer. (B) Spectral PA and PT identification of CNTs using tomato leaves grown in darkness (white) and under light (green). (C) Two-dimensional PT maps (with three-dimensional simulation) of CNT distribution in tomato leaves compared with conventional optical images. Calibration model was constructed by injection of CNTs into leaf. (D) PA detection of CNTs in 1 mm-thick section of tomato fruit. Reproduced with permission from Khodakovskaya *et al.* (17).

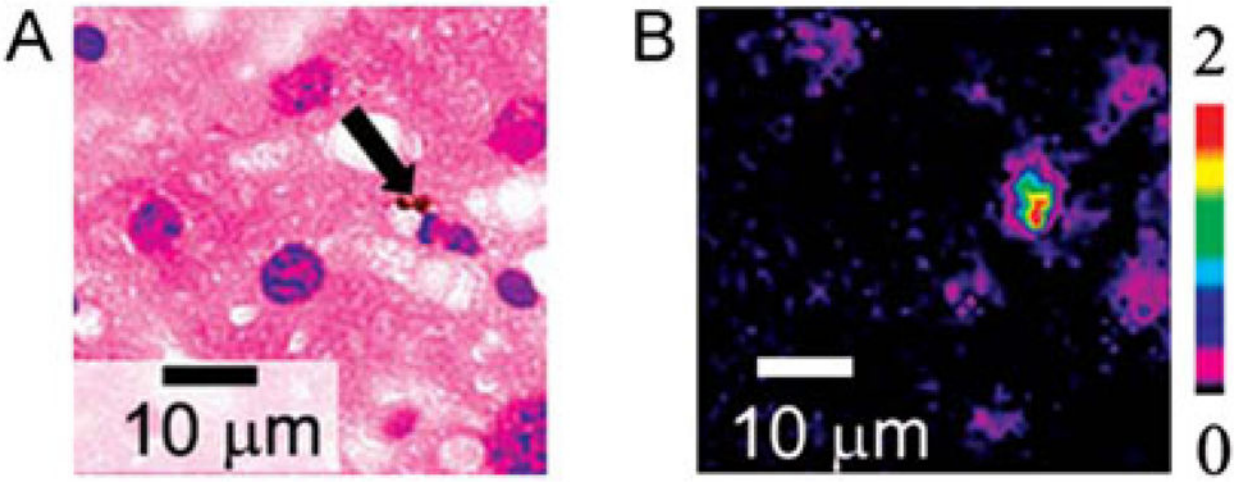

Figure 15.

Optical (left) and photothermal (PT) image (right) of mouse liver histological sample with carbon nanotube (CNTs). PT technique revealed many small (<0.3 μm) CNTs, which were invisible with conventional optical technique. The presence of a few large 1–2 μm CNT clusters (arrow) was used for verification of PT mapping. Laser parameters: wavelength 800 nm, pulse energy fluence 0.1 J/cm^2. Reproduced with permission from Nedosekin *et al.* (16).

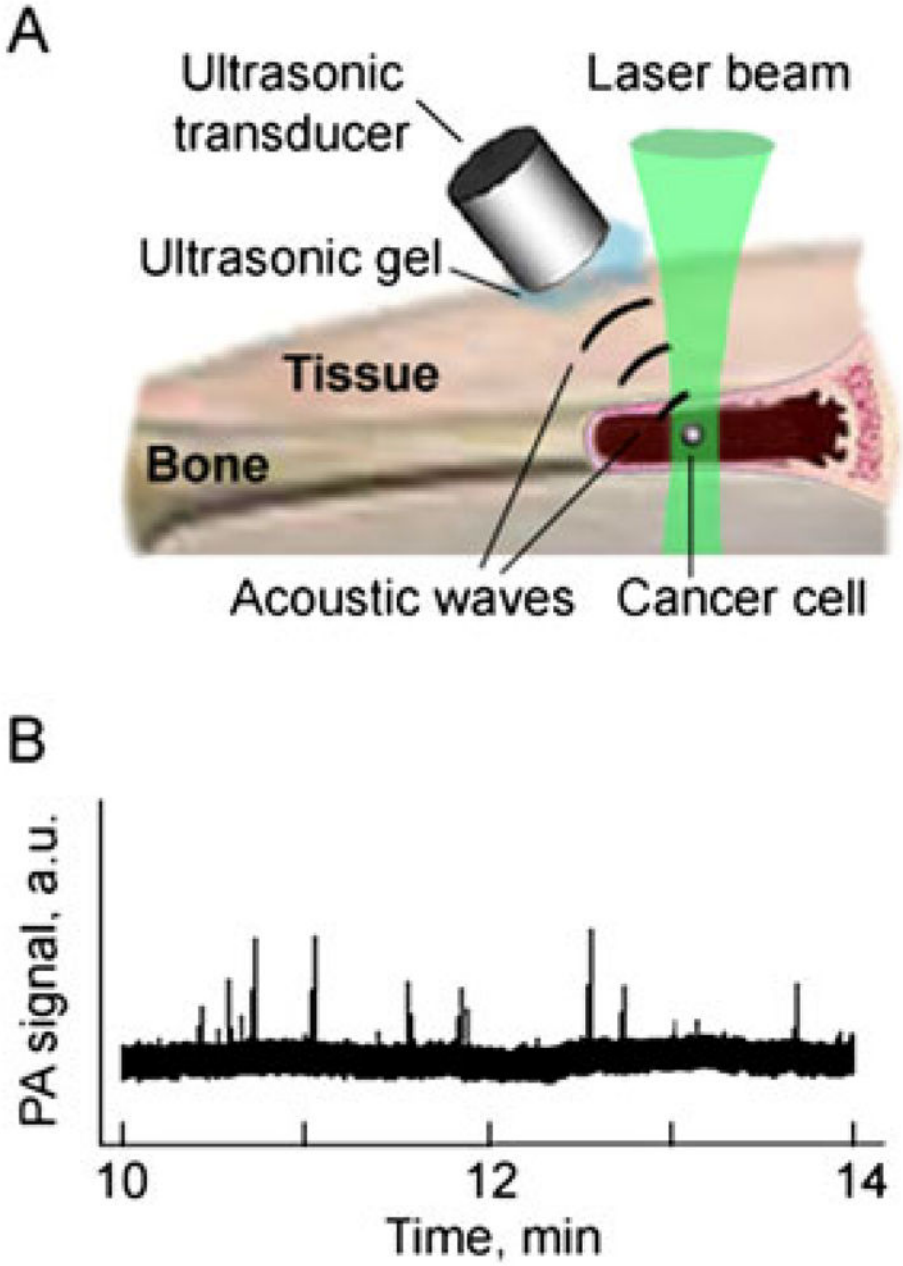

Figure 16.

In vivo photoacoustic bone flow cytometry. (A) Schematics. (B) Noninvasive *in vivo* detection of circulating carbon nanotubes (CNTs) in mouse tibia.

Table 1

Optical absorbance vs weight of indocyanine green, SWNTs and gold nanorods

	Indocyanine green	SWNT 2 × 200 nm (diameter × length)	GNR, 10 × 40 nm (diameter × length)
Peak optical absorbance (cm^{-1} M^{-1})	2×10^5 (58)	6×10^6 (59)	10^9 (60)
Molecular weight (Da)	775	170×10^3	35×10^9
Absorbance/weight (cm^{-1} M^{-1} Da^{-1})	260	35	0.029

SWNT, single-walled carbon nanotube, GNR, gold nanorod.

Table 2

General guidelines for the validation of a targeted PA imaging agent

Test	System	Description/comments	Purpose
PA spectrum	*In vitro*	Measure the PA signal from the imaging agent across a range of possible excitation wavelengths. Only if the agent is nonscattering and nonfluorescent, optical absorbance measurement can be done instead.	Identify the optimal excitation wavelength
Signal-concentration relation	*In vitro*	Quantify the change in PA signal as imaging agent concentration increases	Correlate imaging agent concentration to PA signal
Serum stability	*In vitro*	Measure the physical, chemical and optical integrity of the agent and its PA signal as it is exposed to animal serum	Mimic the enzymatic activity the agent is exposed to in the animal's systemic circulation
Photobleaching	*In vitro*	Measure the PA signal degradation as the agent is exposed to extended durations of light exposure	Mimic laser light exposure of agent in the animal
Cell-uptake study	*In vitro*	Incubation of cells expressing the molecular target with either the imaging agent or the control untargeted imaging agent	Quantify molecular target specificity of the imaging agent
Sensitivity	*In vivo*	Quantify the PA signal from a series of subcutaneous injections of the imaging agent in an animal and compare that to the background signal	Find the lowest detectable concentration (i.e. sensitivity) in living subjects
Targeting capability	*In vivo*	Administration of the targeted imaging agent to diseased animal models (e.g. tumor-bearing mice via intravenous injection) while administering additional animals the control untargeted imaging agent	Answer whether the imaging agent is delivered in a specific way to the target site and in a sufficient amount to produce a detectable signal
Validation	*In vivo* or *ex vivo*	Validate with an independent measure either *in vivo* or *ex vivo*, the delivery of the imaging agent to the target site	Validate the *in vivo* targeting results